Origin, size distribution and hygroscopic properties of marine aerosols in the south-western Indian Ocean: report of 6 campaigns of shipborne observations

Meredith Dournaux[1], Pierre Tulet[1], Joris Pianezze[1], Jérome Brioude[2], Jean-Marc Metzger[3], Melilotus Thyssen[4], and Gilles Athier[1]

[1]LAERO, Laboratoire d'Aérologie (UMR 5560 CNRS, UT3, IRD), Toulouse France
[2]LACy, Laboratoire de l'Atmosphère et des Cyclones (UMR 8105 CNRS, Université de la Réunion, Météo-France), Saint-Denis de la Réunion, France
[3]OSU-R, Observatoire des Sciences de l'Univers de La Réunion (UAR 3365, CNRS, Université de la Réunion, Météo-France), Saint-Denis de la Réunion, France
[4]MIO, Institut Méditerranéen d'Océanologie (UMR 235 Aix Marseille Univ, Université de Toulon, CNRS, IRD), Marseille, France

Correspondence: Pierre Tulet (pierre.tulet@cnrs.fr)

Abstract. ~~Marine aerosol observations from 6 shipborne campaigns carried out in~~ This study presents observations of marine aerosols made during six ship-based campaigns in the southwestern Indian Ocean in 2021 and ~~2023 in the southwest Indian Ocean are presented.~~ 2023. A set of aerosol measurement instruments is used to study the spatial and temporal variability of the ~~aerosol size distribution ,~~ number and size distribution of marine aerosols, the concentration of cloud condensation nuclei (CCN) ~~, activation diameters, and hygroscopicity (~~and the hygroscopic properties of aerosols (Kappa-Köhler κ ~~). Total number of aerosols~~ parameter). It has been shown that the number of submicron aerosols measured varies much more significantly (ranging from 100 to over 3,000 cm^{-3}) than the number of CCN (~~Na) shows concentration above 1500~~ 60 to 500 cm^{-3} ~~in polluted areas,and between 100-1500 in the open ocean. CCN measurements (0.2 %,~~ at 0.4% supersaturation)~~range from 40 to 500 . At 0.2 % (0.4 %)supersaturation, the average activation diameter is 104 (76) nm and~~ . As a result, the κ ~~is 0.36 (0.25) . Using a back-trajectory model,~~ values obtained show considerable variability, ranging from 0.05 to 0.7. Four distinct scenarios are examined to elucidate some of these variations. In the eastern regions of the sampling area, where CCN concentrations are very low (60 to 100 cm^{-3}), the ~~aerosol data were classified into three source regions. Aerosols are hydrophobic in the continental group~~ calculation of the κ parameter is highly variable. These low concentrations probably make the calculation overly sensitive to the method of combining two different instruments. Significant aerosol concentrations above 6,000 cm^{-3} and very low κ values ($\sim$0.1) are observed in the Mozambique Channel. These peaks of weakly hydrophilic aerosols are attributed to the advection of polluted air masses from the upper part of the boundary layer located above the urbanized coastal area of northwestern Madagascar. A temporal decorrelation between maximum aerosol number concentrations, high surface wind speeds and sea state during storm conditions was also observed and attributed to the influence of precipitations. Finally, it has been shown that a sudden increase of the aerosols number concentration observed in a pristine area was caused by the formation of new particles (nucleation) triggered by the passage of the ship through an area of clear skies. The size

distribution of the sampled marine aerosols was analyzed according to the origin of the air masses. In general, a shift of the Aitken and accumulation modes towards larger aerosol sizes was observed for continental and subtropical air masses in the Indian Ocean due to aging. Conversely, the modes shifted towards smaller sizes for air masses in the southern Indian Ocean due to higher primary marine emissions. Aerosols are more hydrophobic for continental air masses (κ ~~from~~ ~0.1~~to 0.13),~~ ~~hydrophilic in the Subtropical Indian Ocean group~~), more hydrophilic and variable over the subtropical Indian Ocean (κ ~~from 0.24 to 0.4) , and intermediate values are found in the Southern Indian Ocean group~~ ranging from 0.2 to 0.6) and intermediate (κ ~~from 0.17 to 0.22) . Subtropical Indian Ocean κ increases with stronger wind speeds. Southern Indian Oceanκ decreases significantly (between 0.2 % and 0.4 % supersaturation) with stronger wind speeds, probably due to a higher concentration of organic species on the smallest particle surface. High aerosol concentration events are presented. Pollution related to air masses passing through a well-developed continental boundary layer. Nucleation triggered by clear skies between two cloudy periods. Arrival of air masses at the ship's location after a precipitation event.~~ ~0.2) over the southern Indian Ocean. The κ of the subtropical Indian Ocean increases with wind intensity, while it remains stable in the southern Indian Ocean. This effect is attributed to the high proportion of primary organic matter, which is due to the important concentration of nanophytoplankton in the southern Indian Ocean. It has been shown that primary organic aerosols act as surfactants, thus counterbalancing the highly hydrophilic properties of NaCl.

1 Introduction

Aerosols have been identified as playing a key role in climate, cloud formation, and cloud lifetime through their direct and indirect effect (IPCC, 2013, 2021; Wall et al., 2023). Among them, marine aerosols constitute a significant mass proportion of particles with global emissions estimated between 2,000 to 10,000 Tg year^{-1} (O'Dowd et al., 1997; Bates et al., 2005; Textor et al., 2006; de Leeuw et al., 2011). Marine aerosols are defined as aerosols comprising all types of particles found over the oceans, regardless of their point of origin. Some come from local sources and are either mechanically injected into the atmosphere via bubble bursting (Lewis and Schwartz, 2004; de Leeuw et al., 2011), wave crest tearing (Monahan et al., 1986), or chemically formed by gas to particle conversion after gas emission from the ocean essentially due to phytoplankton activity (Saltzman, 2009; de Leeuw et al., 2014). Others come from remote sources and are transported from landmasses towards the ocean as dust (Schulz et al., 2012), biomass burning aerosols, or particles originating from fossil fuel combustion (Ramanathan et al., 2001; Novakov et al., 2000). This diversity of origins makes the size and chemical composition of marine aerosols highly variable. These two characteristics are essential in determining the aerosol hygroscopicity, which is the ability of aerosols to take up the surrounding atmospheric water vapor and grow to larger sizes. Thus, according to their hygroscopicity, marine aerosols may act as cloud condensation nuclei (CCN) and activate as cloud droplets leading to cloud formation (Köhler, 1936). Clouds in turn affect the Earth's energy balance by reflecting short-wave radiation and absorbing and emitting long-wave radiation. Indeed, a change in aerosol concentration or its properties affects cloud droplet number concentration (Twomey, 1974, 1977) and cloud lifetime leading to changes in precipitation (Albrecht, 1989). For instance, low clouds, such as marine stratocumulus, which is the most widely spread cloud type on Earth (Warren et al., 1988, 2007), ~~has~~ have been intensively

studied due to their strong sensitivity to aerosol concentration changes, which affect their cloud droplet number (Stevens et al., 1998; Sandu et al., 2008; Brioude et al., 2009; Jia et al., 2019). Therefore, the complex interactions between aerosols and these clouds in the marine environment constitute one of the largest uncertainties in climate models (Carslaw et al., 2013; Simpkins, 2018) and contribute to less accurate climate predictions. One of the primary reasons for these uncertainties ~~lie~~ lies in the inadequate depiction of aerosol sources in the remote marine ocean (Carslaw et al., 2017). In this region where aerosol loads are the lowest, cloud droplet sensitivities are the greatest (Moore et al., 2013).

To improve our understanding of the life cycle, size distribution, and chemical composition of marine aerosols and their impact on climate; several studies were conducted mainly in the Atlantic, ~~the~~ Pacific, and ~~the~~ Northern Indian oceans (Heintzenberg et al., 2000). Some studies focused on the physical properties of marine aerosols ~~. Flores et al. (2020) provided recent marine aerosol total number concentration and size distributionmeasurements along coastal and remote areas of the Pacific and the Atlantic oceans during the Tara Pacific Expedition (2016-2018). In the open ocean and far from continental sources, the average Na (0.03-10) was~~ and reported a wide range of number concentration associated with a variable size distribution. For instance, Flores et al. (2020) measured strong differences in aerosol number concentrations, with an average of 180 ± 51 cm^{-3} in the Pacific Ocean and 864 ± 806 cm^{-3} in the ~~Pacific and Atlantic Oceans respectively. The associated size distributions were bimodal with an Aitken mode median diameter between 30-50 nm and an accumulation mode median diameter around 200 nm. Under continental influence, Na exceeded 5000~~ Atlantic Ocean. Under the influence of an air mass of continental origin the number of aerosols can reach several thousand particles per cm^{-3} ~~in the Atlantic Ocean and 2718 ± 1560 on average in the western Pacific Ocean. The associated size distributions were monomodal with a mean diameter around 100 nm. In the Indian Ocean, Pant et al. (2009) measured Na and its size distribution (16-700 nm and 0.5-20 in diameter) from 14° N to 56° S (January-March 2004). They reported a minimum concentration of micrometer aerosols in the trade wind region around 11° S and a bimodal size distribution with an Aitken mode mean diameter around 50 nm in addition to an accumulation mode mean diameter around 130 nm. North and south of the trade wind region, the concentration of micrometer particles was higher, and the maximum concentration (5.8 ± 3.5) was recorded in the roaring forties from 40°-56° S. South of the trade wind region the aerosol number size distribution was more monomodal with a higher number concentration of aerosols in the Aitken mode.~~ (Flores et al., 2020).

Other studies focused on the ~~chemical composition of aerosols. In the Northern Atlantic Ocean and along the Northern American shores, Kasparian et al. (2017) showed that the organic fraction of aerosols was higher (reaching up to 10 % of the aerosol compositionbetween 30-32 PSU and 12-14°C) over colder and less salty waters outside of the Gulf Stream compared with warm and salty waters within the Gulf Stream.~~ variability of the aerosols chemical composition. For instance, Yoon et al. (2007) investigated seasonal chemical composition of marine aerosols in the North Atlantic Ocean and found a maximum ~~(minimum)~~ mass concentration of ~~sea salt in the supermicron~~ NaCl in the coarse mode during winter ~~(summer)~~ due to stronger wind speeds during this season. ~~On the contrary, non sea-salt~~ In contrast, they measured a higher sulfate concentration in ~~the submicron mode exhibited higher concentration during summer than winter. Several studies conducted both in the field or in laboratory (O'Dowd and de Leeuw, 2007; Christiansen et al., 2019) have been dedicated to the physical mechanisms generating sea spray aerosols .~~ summer than in winter in the submicrometer mode. In the eastern part of the Atlantic Ocean,

O'Dowd et al. (2004) and Cavalli et al. (2004) observed a significant fraction of organic matter in primary marine aerosols, which they explained by the presence of phytoplankton blooms. During a phytoplankton bloom, Facchini et al. (2008) observed an increase in the organic fraction of primary marine aerosols from 3 % to 77 %, while the diameter of the particles decreased from 8 µm to 125 nm. On Amsterdam Island, during summer, Sciare et al. (2009) also observed a peak in the organic fraction of primary marine aerosols (> 250 $\mathrm{ng\ m^{-3}}$), which they related to a region of high concentration of Chlorophyll-a located between 1,000 and 2,000 km from the measurement site. Sciare et al. (2009) also observed a higher concentration of black carbon in marine aerosols during winter (7 - 13 $\mathrm{ng\ m^{-3}}$) than during summer (2 - 5 $\mathrm{ng\ m^{-3}}$). They explained this increase in the black carbon fraction by the transport of pollution plumes from South Africa and Madagascar (fires and combustion of fossil fuels).

Other studies focused on CCN number concentration. In the Southern Ocean, Quinn et al. (2017) identified a large portion of Aitken mode particles acting as CCN at ~~SS >~~ supersaturation (SS) greater than 0.5 %. In the Southern Ocean, Tatzelt et al. (2022) reported shipborne CCN number concentrations ranging between ~~3-590~~ 3 - 590 $\mathrm{cm^{-3}}$ at 0.3 % SS in the austral summer during cruises conducted between the southern tips of Argentina, South Africa, and Australia. At the same SS, Sanchez et al. (2021) reported airborne CCN measurements conducted in the marine boundary layer (MBL) ranging from 17 to 264 $\mathrm{cm^{-3}}$ between Tasmania and ~~62°~~ 62° S in the austral summer.

Marine aerosol hygroscopicity (materialized by the Kappa-Köhler parameter, κ) has been prescribed to a single value of 0.7 $\pm$ 0.2 (Andreae and Rosenfeld, 2008), or 0.72 $\pm$ 0.24 according to global model simulation (Pringle et al., 2010). However, several field campaigns reported a large variability of κ values according to the influence of air masses and the presence of marine biologic activity. For instance, ~~Huang et al. (2022) studied the spatial variation of marine aerosol (≤ 300 nm in diameter) κ over 100° of latitude in the Atlantic ocean. They measured κ~~ values ranging from 0.14 to 0.16 were measured in the equatorial region of the Atlantic ocean which is influenced by biomass burning emissions coming from Africa ~~and characterized by~~ wind speeds smaller than 4 ~~m~~ $\mathrm{m\ s^{-1}}$ (Huang et al., 2022). In comparison, ~~regions with air masses coming from the ocean~~ κ values ranging from 0.86 to 1.06 were measured in regions influenced by oceanic air masses and characterized by ~~strong wind speed (≥~~ wind speed greater than 10 ~~m)~~ $\mathrm{m\ s^{-1}}$ (Huang et al., 2022).

At Barbados, accumulation mode particles were associated with ~~higher~~ κ values ~~ranging from 0.86 to 1.06 for 300 nm particles. Jung et al. (2013) reported κ values~~ as low as 0.02-0.03 ~~for accumulation mode particles~~ during an intense Saharian dust episode ~~arriving at Barbados. In the same area, but without the influence of Saharian dust, Wex et al. (2016) reported an average κ~~ (Jung et al., 2013), while an average value of 0.66 ~~for particles in the size range 50-200 nm, indicating the~~ was reported by Wex et al. (2016) which they explained by the presence of sulfates generally formed during ~~new particle formation events. In the summermonth at Barbados, Kristensen et al. (2016) reported~~ nucleation events. During summer, a decrease in κ values ~~in the range~~ was observed (0.2-0.5~~for supersaturations between 0.1-0.7 %, and attributed these low values to~~) and explained by the presence of a significant organic volume fraction in the ~~particles ranging between 50-200 nm, confirmed by transmission electron microscopy evaporation studies. Shipborne measurements performed in the tropical Atlantic Ocean between Portugal and Cape Verde exhibited κ between 1.15-1.4 for marine air masses, κ between 0.92-1.24 for African air masses, and κ between 0.75-0.89 for continental air masses (Good et al., 2010). Within the marine boundary layer west of~~

~~the North American coast, Roberts et al. (2010) reported an average κ value of 0.21 at 0.35 % supersaturation for air masses that originated from the North Pacific Ocean.~~ accumulation mode particles (Kristensen et al., 2016). In the Southern Ocean, between Tasmania and ~~62° S,~~ 62° S, Sanchez et al. (2021) reported a wide range of κ values~~exhibit a large variability ranging between 0-1.2 (Sanchez et al., 2021), according to the processes impacting the air mass history (aging, recent particle formation and aging, scavenging, recent particle formation and scavenging). In this study, κ values also varied according to the latitudes, with higher values (κ ~~–~~, between 0 and 1.2. The highest values ($\kappa \sim 1$) were found at lower latitudes ~~due to primary emissions, and lower values~~ and explained by primary emissions. κ values ranging from 0.6 to 0.9 were found at higher latitudes ~~(κ between 0.6-0.9 in~~ in the presence of sulfate species~~and~~ , and the lowest values ($\kappa < 0.2$~~in presence of~~) were explained by organic species from biogenic emissions~~).~~ .

However, few studies attempted to link marine aerosol number concentration, size distribution, and hygroscopic properties in the ~~Southern~~ southern Indian Ocean and the Southern Ocean. Additionally, most of the campaigns already carried out were short-term field campaigns, targeted specific remote or coastal regions, and used different instrumentation from one expedition to another; leading to the generation of unmatched data sets.

The Marion Dufresne Atmospheric Program-Indian Ocean (MAP-IO) was launched in 2021 (www.mapio.re; ~~(Tulet et al., 2024)~~ Tulet et al. (2024)). The program relies on continuous atmospheric and oceanic measurements realized aboard the Marion Dufresne II vessel (https://taaf.fr/collectivites/le-marion-dufresne/) over the Southern Indian Ocean. One of its objectives is to better characterize the properties of marine aerosols (i.e. their number concentration, size distribution, and hygroscopic properties) in a poorly documented area far from the main anthropogenic influences. One particularity of MAP-IO is that it uses the same vessel and the same instrumentation~~over~~, to the authors knowledge, over the longest sampling period and greatest spatial coverage ever undertaken in this region. Each year the Marion Dufresne covers a large panel of latitudes extending from the sub-equatorial region until the subantarctic front (~~20°~~ 20° S – ~~60°~~ 60° S). This offers various possibilities to study the impact of local in-situ conditions on marine aerosol size distribution and hygroscopic properties. This includes weak to strong wind speeds, calm to rough ocean, sunny to cloudy areas, regions of intense biological activity, pristine areas, and coastal zones influenced by human activity. The large spatio-temporal coverage also allows us to capture large-scale influence via long-range transport of aerosols over the Southern Indian Ocean. This diversity is translated in the great spatial and temporal variability of ~~Na~~ aerosol number and size distribution of marine aerosols observed during campaigns that took place between 2021 and 2023 and presented in Tulet et al. (2024). Complementary measurements involving a photometer, an automated flow cytometer, and gas analyzers allow to identify terrestrial transport and any relation with phytoplankton distribution and functional composition.~~The objective~~

The aim of this paper is to present the variability of ~~marine aerosol hygroscopicity and size distribution over the eastern and southern Indian Ocean. Six oceanographic campaigns are used to provide the spatio-temporal distribution of marine aerosol size distribution and their hygroscopicity from SMPS, OPC-N3, and CCN-100 analyzers. As aerosol hygroscopicity is closely linked to their chemical composition which in turn depends on local and large-scale conditions, we propose to use co-located measurements of wind speed, wave height, gases, phytoplankton functional groups distribution, and back trajectories simulations to analyze the differences in the calculated hygroscopicity.~~ the size distribution and hygroscopicity

of marine aerosols based on six shipboard observing campaigns in the Indian Ocean, representing 192 days of measurements. The observations are presented according to their spatial distribution, then four particular situations are analyzed to illustrate the origin and the large variability of the measurements. The paper then aims to provide a synthetic representation of the size distribution and hygroscopicity of marine aerosols as a function of the continental, subtropical, or southern Indian Ocean origin of the sampled air masses.

This paper is organized as follows: ~~section~~ Section 2 is dedicated to the presentation of the campaigns, and the in situ conditions encountered. Section 3 describes instrumentation and section 4 focuses on data processing. Section 5 deals with the spatial and temporal variability of marine aerosols properties. Section 6 ~~presents the origin of analyzed~~ focuses on particular events. Section 7 presents the aerosol size distributions according to the origin of air masses, ~~section 7 focuses on particular events, and conclusions and~~ and the evolution of aerosol hygroscopicity according to wind speed and nanophytoplankton abundance. Conclusions and perspectives are presented in ~~section~~ Section 8.

2 Campaigns overview and in situ conditions observed

2.1 Campaigns overview

Between January 2021 and March 2023, MAP-IO carried out a total of ~~16~~ sixteen campaigns aboard the Marion Dufresne, including ~~6~~ six during which the aerosol instruments performed well and are presented in this article (Fig. 1, Table 1). During these ~~6~~ six campaigns, the spatial coverage of the Marion Dufresne extended from latitudes ~~-10.65° S to -60°~~ −10.65° S to −60° S and longitudes ~~31° E to 83.2°~~ 31° E to 83.2° E and thus encountered various environmental conditions (Fig. ~~??).~~ 1). The start and end dates of the various campaigns and the instruments used are shown in Table 1.

The SWINGS campaign (Fig. 1~~,~~; blue track) took place during the austral summer from January ~~13th to March 8th.~~ 13 to March 8, 2021. The aims were to collect ~~CO2~~CO_2, pH, and fish population density measurements at different latitudes and depths in the ~~Southern~~ southern Ocean. During this campaign, the Marion Dufresne route begins along coastal regions passing south of Madagascar and southeast of Africa, then moves on to open ocean where it stops at ~~Crozets then Kerguelen islands~~ Crozet then Kerguelen Islands before returning to Reunion ~~island~~Island. The SCRATCH campaign (Fig. 1~~,~~; red track) took place during austral winter and was carried out from July ~~1st to 22nd.~~ 1 to 22, 2021. The aim was to better characterize the region using a combination of biological and geological techniques. During this campaign, the vessel passed east of Madagascar and stayed in the northern part of the Mozambique Channel before going back to Reunion ~~island~~Island. The MAYOBS campaign (Fig. 1~~,~~; green track) was carried out during austral winter from September ~~13th to October 3rd,~~ 13 to October 3, 2021, as part of the monitoring of an underwater volcanic eruption that began around Mayotte in 2018. The route of the vessel was similar to the one during the SCRATCH campaign. The OP3 and OP4 campaigns (Fig. 1~~,~~; orange and lime tracks) were carried out under TAAF charter during austral spring from October ~~28th to November 28th,~~ 28 to November 28, 2021, and from November ~~28th to December 30th~~ 28 to December 30, 2021, respectively. During these two campaigns, the Marion Dufresne took the same routes: Reunion ~~island-Crozets islands-Kerguelen islands-Amsterdam island-Reunion island~~Island-Crozet Islands-Kerguelen Islands-Amsterdam Island-Reunion Island. The OBSAUSTRAL campaign (Fig. 1~~,~~; purple track) took place during the aus-

tral summer in 2023 from January ~~18th to February 28th.~~ 18 to February 28. The objectives were the same as the SWINGS campaign, including the monitoring of seismic activity at ocean ridges and the identification of cetaceans vocal signature using hydrophones. The vessel route was similar to the one during OP3 and OP4 with one exception: it went further to the south between ~~Crozets islands and Kerguelen islands~~ Crozet Islands and Kerguelen Islands and further to the east between Amsterdam ~~island and Reunion island~~Island and Reunion Island.

2.2 Atmospheric and oceanic conditions observed

Between ~~10° S and 25°~~ 10° S and 25° S, westward surface atmospheric and oceanic circulation are prevailing with southeast equatorial winds and the South Equatorial Current (SEC) ~~. Between Madagascar and 80° E during summer~~ (Fig. 1~~red arrows), surface winds are weaker and slightly oriented west to northwest. During winter, (Fig. 1 blue arrows) surface winds are stronger and oriented northwest ((Schott et al., 2009), and references therein).~~). In this latitude range, the average wind speed measured onboard the Marion Dufresne is ~~8.9~~ 6.7 ± ~~4.6 m~~ 3.9 $\mathrm{m\,s^{-1}}$ (Fig. 2a), the average wave height is ~~4.5~~ 2.5 ± ~~2.3 m~~1.2 m (Fig. 2c), and the average nanophytoplankton abundance is ~~669.1~~ 306.1 ± ~~583.7 cell~~ 90.2 $\mathrm{cells\,cm^{-3}}$ (Fig. ~~2~~2c). Madagascar~~'~~'s high plateaus play a role in regional circulation by splitting the trade winds into two branches. A northeasterly flow, which notably affected the region of the SCRATCH and MAYOBS campaigns. A southeasterly flow, which affected the beginning of the SWINGS campaign~~'~~'s route between Reunion Island and Madagascar. The oceanic circulation also divides into two branches at the northeastern tip of Madagascar with one bypassing the island to the north (North East Madagascar Current, NEMC) and the other to the south (South East Madagascar Current, SEMC) (Fig. 1). ~~These two currents contribute to the development of the Mozambique Channel eddies west of Madagascar.~~ Between the southern tip of Madagascar and ~~30°~~ 30° S, the wind direction progressively changes and becomes eastward when encountering strong westerlies typically extending from ~~35° S to 60° S .~~ 35° S to 60° S (Fig. 1). The SEMC flows towards the southeast coast of Africa where it becomes the Agulhas Current (AC) ~~. Although the southeast coast of Madagascar is an oligotrophic region, phytoplankton blooms occur in January and April and can extend over 2500 eastward (Longhurst, 2001; Dilmahamod et al., 2019). However, during the sampled period, no enhancement of the phytoplankton abundance was observed in this region during the SWINGS campaign~~ (Fig. ~~2~~c1). The area extending southeast of Madagascar has rather been considered as pristine in the literature (Fig. 1; blue shaded area) (Mallet et al., 2018). At ~~40°~~ 40° S, the AC is retroflected and goes eastward. Then it becomes the South Indian Current (SIC) and flows northeastward ~~.~~ (Fig. 1). The subantarctic front is located south of it~~, with the northern Subantarctic front typically between 45° S and 50° S and the southern Subantarctic front located between 50° S and 60° S~~. This current is characterized by a strong sea temperature and salinity gradient between the Subtropical zone and the Antarctic zone which marks the northern boundary of the Southern Ocean (Giglio and Johnson, 2016). The Marion Dufresne crossed the subantarctic front during the SWINGS, OBSAUSTRAL, OP3, and OP4 campaigns. In this area, phytoplankton blooms driven by nitrate, phosphate, or iron water fertilization were observed during the austral summer on the Crozet Islands (~~46° S, 51°~~ 46° S, 51° E) and Kerguelen Plateau (~~49° S, 69°~~ 49° S, 69° S) (Sedwick et al., 2002; Blain et al., 2008). Measurements of nanophytoplankton abundance were performed during SWINGS and OBSAUSTRAL, during the austral summer, and showed a clear signal of enhancement between ~~40-55°~~ 40° - 55° S (Fig. 2c). The polar front is further in the south between ~~55° S and 60°~~ 55° S and 60° S and

marks the boundary between the warmer subantarctic water and the cold Antarctic water. The Southern Ocean is the roughest ocean on Earth due to the absence of land (Young, 1999). Even in the austral summer, Derkani et al. (2021) measured average wind speeds of 11 ~~m~~ $\mathrm{m\,s^{-1}}$ and swells in excess of 3.5 ~~m~~m. During the SWINGS and OBSAUSTRAL campaigns, average winds also exceeded 10 ~~m~~ $\mathrm{m\,s^{-1}}$ and average wave heights exceeded 5 ~~m~~m. Three major storms were documented during the SWINGS campaign in ~~2021.~~ 2021 (Fig. 1a; black circles). The first one located south of ~~Crozets islands~~Crozet Islands, the second one south of Kerguelen ~~islands~~ Islands and the third one north of Kerguelen ~~islands~~Islands. The maximum wind speed was respectively 23 ~~m~~ $\mathrm{m\,s^{-1}}$, 33 ~~m~~ $\mathrm{m\,s^{-1}}$, and 27 ~~m . The~~ $\mathrm{m\,s^{-1}}$. The predominant wind direction was from the northwest south of Crozet Islands and Kerguelen Islands, and from the southwest north of Kerguelen Islands (Fig. 2b). The maximum wave height was ~~respectively~~ 14 ~~m~~m, 21 ~~m~~m, and 15 ~~m.~~ m, respectively (Fig. 2c). The nanophytoplankton abundance ~~is~~ was lower (400-800 ~~cell mL~~ $\mathrm{cells\,cm^{-3}}$) along the storm tracks (Fig. 2d) due to a more ~~important mixing which deepens~~ intense mixing that deepened the ocean mixing layer, and ~~limits~~ limited the light available for phytoplankton growth (Fragoso et al., 2024).

It is important to note that the local wind direction observed during the campaigns is highly variable and differs from the general wind circulation presented in Figure 1. Therefore, in order to conduct a thorough analysis of particular periods within the campaigns, it is imperative to pay close attention to the local measurements of wind. For more information on the climatology of the ~~south-western~~ southwestern Indian Ocean and the Southern Ocean, see for example the studies by Schott et al. (2009) or Mondal et al. (2022).

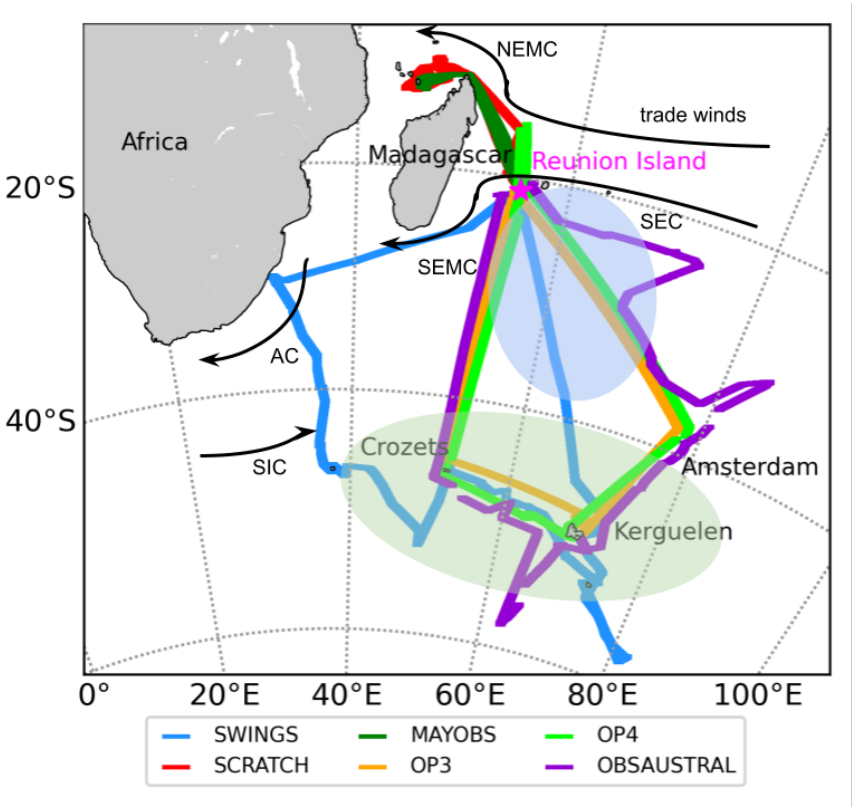

Figure 1. Marion Dufresne paths colored by campaign in 2021 and 2023 during four specific campaigns (SWINGS, SCRATCH and MAYOBS 2021, OBS AUSTRAL 2023) and two port operations (OP3 and OP4 2021). ~~Filtered data is colored according to the campaigns whereas black solid lines present the total path of the Marion Dufresne before filtering.~~ Paths of OP3, OP4, and OBSAUSTRAL are shifted in longitude (between ~~-1.4°~~ $-1.4°$ and ~~1.2°~~$1.2°$) and latitude (between ~~-1.6°~~ $-1.6°$ and ~~1°~~$1°$) from their original location to give a better view of the different campaigns. Black arrows represent the surface atmospheric and surface oceanic circulation in the region. Green shaded area is the region where phytoplankton are the most abundant and are generally observed in the austral summer. Blue shaded area is the pristine region observed in the ~~Southern~~ southern Indian ocean.

Name of campaign	Start to end date	Analyzed data
SWINGS	2021-01-13 to 2021-03-08	~~CPC,~~ SMPS, OPC-N3, CCN-100
SCRATCH	2021-07-01 to 2021-07-22	SMPS, OPC-N3, CCN-100
MAYOBS	2021-09-13 to 2021-10-03	SMPS, OPC-N3, CCN-100
OP3	2021-10-28 to 2021-11-28	SMPS, OPC-N3, CCN-100
OP4	2021-11-28 to 2021-12-30	SMPS, OPC-N3, CCN-100
OBSAUSTRAL	2023-01-18 to 2023-02-28	CPC, SMPS, OPC-N3, CCN-100

Table 1. Name and duration of the campaigns realized in 2021 and 2023 and list of data analyzed in the present paper.

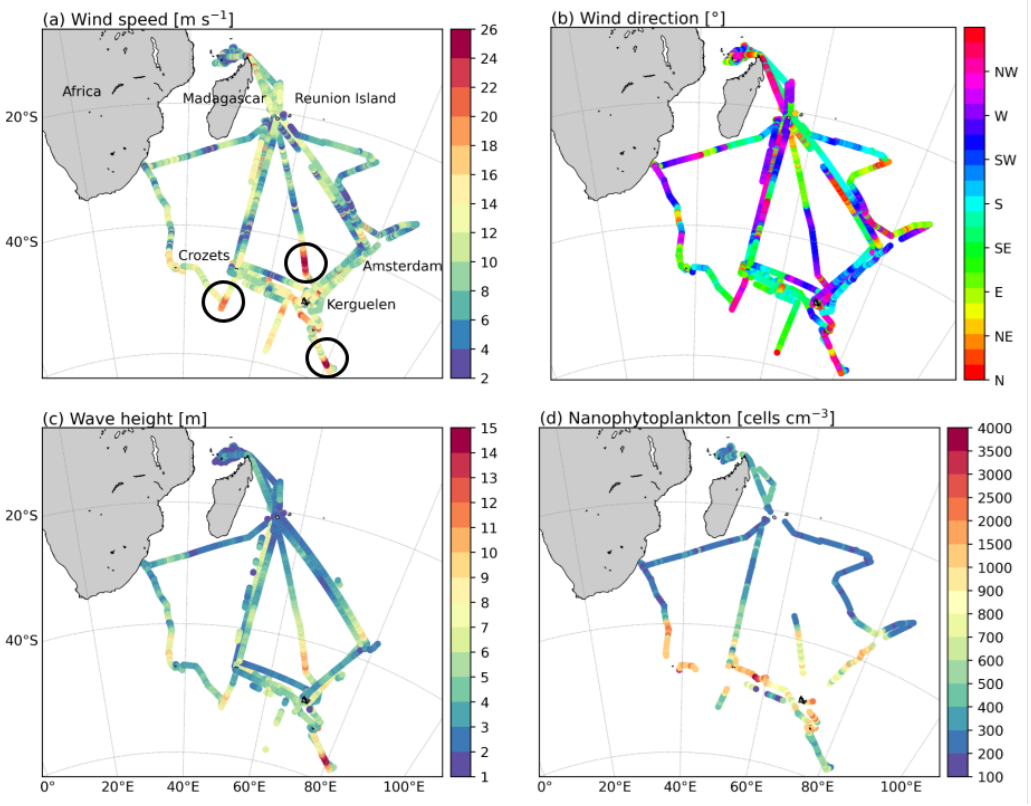

Figure 2. Marion Dufresne path colored by ~~wind speed~~ (a) wind speed, ~~wave height~~ (b) wind direction, ~~and nanophytoplankton abundance~~ (c) wave height, and (d) nanophytoplankton abundance during the six campaigns analyzed. The three storms that occurred during SWINGS are circled in black.

3 Instrumentation description

In the framework of the MAP-IO program, the Marion Dufresne has been equipped with ~~19~~ nineteen measurement and remote sensing instruments described in Tulet et al. (2024). Among the ~~19 instruments, 7~~ nineteen instruments, seven are dedicated to the study of aerosols and atmospheric gas. In Figure 3, top left and right pictures present the aerosol and gas inlets located at the center of the vessel, upstream of the exhaust stack and 21 m above the sea level. The bottom picture of Figure 3 shows the aerosol and gas acquisition system and analyzers located in the meteorological laboratory and mounted on a shock-absorbing table.

Figure 3. Picture of the Marion Dufresne in the Port-aux-Français Bay (February 2024). ~~The aerosol~~ (a) The aerosol and ~~gas inlets~~ (b) gas inlets are located above the wheelhouse. (c) The acquisition and monitoring system ~~(c)~~ is located in the meteorological room, next to the wheelhouse and mounted above a shock-absorbing table. Aerosol monitoring systems are on the top shelf, right of the acquisition computer. Gas analyzers are on the bottom shelf. Photography credits: Meredith Dournaux.

Aerosol inflow enters the same sampling line which divides after a Nafion tube, used to dry the aerosol inflow, and direct them towards the different instruments. The distance between the inlets and the instruments (8 ~~m~~m) was carefully chosen to minimize aerosol losses along the sampling line. To minimize the loss of the largest particles (> 1 µm), three OPC-N3 are installed directly outside on the main deck. A Water-Based Condensation Particle Counter (CPC, model MAGICTM-200/210) measures particle number concentration within the size range 5 ~~nm~~ nm to 2.5 µm using a condensational growth system. A Scanning Mobility Particle Sizer (SMPS, model 4S) is used to measure the number size distribution of aerosols. It is composed of a Differential Mobility Particle Sizer (DMPS) and a CPC (model MAGICTM-200/210). The DMPS takes in the aerosol flow composed of dry particles and cloud droplets, the water of the latter is evaporated while penetrating the inlet. The aerosol

population is first neutralized using an X-ray neutralizer (TSI, model) to provide the same electrical charge to all the particles, then selected using their size dependent electrical mobility and classified into ~~80 bins from 20 nm~~ 133 bins from 3 nm to 350 ~~nm~~nm. The number of aerosols per bin is then determined by the CPC. The whole size range is scanned in five minutes.

To complete the aerosol size distribution towards super-micron diameters, three Optical Particle Counters (OPC-N3, model Alphasense) are used to measure the number concentration and the size of particles within the size range 0.35 µm to 40 µm. Using a calibration based on Mie theory, the OPC-N3 measures the light scattered by each particle of a sample air flow (sample flow rate of 210 ~~mL)~~ mL min^{-1} passing through a 658 ~~nm~~ nm laser beam. According to the intensity of the scattered light the particles size and concentration are determined, and permit the classification of each particle into one of the 24 bins covering the measurement size range at a rate of about 10,000 particles per second. Generally, 100 % of the particles are detected at 0.35 µm and 50 % at 40 µm. (Alphasense User Manual, www.alphasense.com). In our case, as the OPC-N3 have no sampling line and are directly located outside, there is no loss of large aerosols except on the walls of the instruments. To study the aerosol activation properties a Cloud Condensation Nuclei Counter (CCN-100, DMT) is used to measure the number concentration of activated aerosols at different supersaturation (SS = 0.1, 0.2, 0.3, 0.4, 0.5, 0.6, 0.8, and 1.0 %), the two first set for fifteen minutes and the others for five minutes. Supersaturation is created by a three temperature control zones column mounted vertically. ~~The temperature at the column wall increases gradually from the top to the bottom to create supersaturation. The~~ The aerosol sample enters at the top of the column and becomes progressively supersaturated with water vapor as it goes through the column. ~~As the sample temperature is lower than the wall temperature and using the fact that water vapor diffusion in the air is faster than heat diffusion, water vapor condenses on particles to form droplets.~~ Activated droplets are then counted by an internal OPC and distributed into 20 size bins going from 0.75 µm to 10 µm. Gas measurements are realized by a ~~NOx~~ NO_x analyzer (model Teledyne N500 CAPS), an ~~O3~~ O_3 analyzer (model HORIBA APOA-370), and a Picarro analyzer (model Picarro G2401 CFKADS-2372) measuring atmospheric gas traces as CO, ~~CO2, CH4, and H2O~~ CO_2, CH_4, and H_2O (ppb). The gas inlets are located right of the aerosol inlet (Fig. ~~2~~3b). Along with aerosol measurements, wind speed, and wind direction (~~m and °~~ $\mathrm{m\,s}^{-1}$ and °), air temperature (~~°C~~°C), pressure (~~hPa~~ hPa), and humidity (%) are recorded by the Vaisala and Mercury meteorological stations with a sampling time step of ~~5 seconds and 1~~ five seconds and one minute respectively. Sea surface elevation (~~m~~m) and ship position is also recorded by the inertial unit of the ship at a sampling time step of ~~1~~ one second.

4 Data processing

4.1 Filtering steps

First the data is filtered to remove all the measurements likely to be contaminated by the exhaust of the vessel. Observations of time series of the total number concentration and the relative wind direction concluded that measurements realized within the direction range ~~90°-225°~~ 90° - 225° were associated with high aerosol concentrations (> ~~5000~~ 5,000 cm^{-3}) lasting in time. A second filter combining relative low wind speed, vessel cruise speed, and gas concentration data was applied in an attempt to remove local episodes of pollution. Thus, all data collected at a wind speed smaller than 2 ~~m~~ $\mathrm{m\,s}^{-1}$ which may have

inhibited pollution plume dilution around the inlets, were removed. In addition, data was removed when the ship was stationary, thus eliminating contamination by maintenance activities on board (painting, rust removal). To complete the filter, data with corresponding high concentrations of NO and ~~NO2~~ NO_2 (> ~~1 ppbv~~1 ppbv) were removed, the latter being relatively low (~~less than 1 ppbv~~< 1 ppbv) in remote marine environments. CO peaks of concentration were also identified following the semi-automatic method of detection described in El Yazidi et al. (2018). The use of different chemical tracers was not only useful when one of the analyzers did not work properly, but also allowed to confirm the good agreement between ~~NOx~~ NO_x and CO concentrations. A third step consisted in the quality control of the aerosol data. For SMPS data, the particle size distributions were filtered manually for each measurement to remove non physical variations (e.g. local pollution undetected by the dynamic and the chemical filters). The latter were noticeable by a brutal and short increase in the concentration of aerosols over the entire range of diameters known as "spikes." SMPS data were quality controlled and corrected over the sampling periods using CPC data. ~~For CCN-100 data, supersaturations of 0.2 % and 0.4 % were treated separately and only the data recorded on plateau (measurements realized approximately three minutes after a supersaturation change according to the CCN-100 manual guide) were averaged over five minutes to make them comparable to SMPS data.~~

The original raw SMPS dataset was made of ~~55144~~ 55,144 measurements of aerosols which represents ~~~~192 days of measurements. After the first and second filtering steps, it consisted of ~~53201~~ 53,201 measurements. After the manual filtering step, ~~36226~~ 36,226 measurements are conserved which represents ~~~~66 % of the original dataset. In total, there were ~~29376~~ 29,376 measurements taken in 2021 and ~~6850~~ 6,850 measurements in 2023 as shown in ~~Fig.~~ Figure 1. The start and end date of each campaign is resumed in Table 1. The data collected in 2022 were not used in this study due to SMPS maintenance and calibration.

4.2 Calculation of activation diameter and hygroscopicity parameter

First, the CCN-100 data at 0.2 % and 0.4 % supersaturation were treated separately and only the data recorded on plateau (measurements realized approximately three minutes after a supersaturation change according to our experience) were averaged over five minutes to make them comparable to SMPS data. Assuming that aerosols are internally mixed and that larger particles are activated preferentially before the smallest ones due to the curvature effect, we can determine the hygroscopicity of aerosols at the activation diameter by calculating activation diameters and deriving the hygroscopicity parameter at both supersaturation. Activation diameters were then calculated using the total number of cloud condensation nuclei given by the CCN-100 and the number concentration of aerosols measured in each bin by the SMPS. The number of aerosols per bin were integrated from the largest diameter towards the smallest until matching the number of CCN. The activation diameter corresponds to this smallest diameter. Hygroscopicity parameter Kappa-Köhler was derived from the previously determined activation diameters as follows (Petters and Kreidenweis, 2007):

$$\kappa = \frac{4A^3}{27D_d^3 \ln^2 \mathrm{S_c}} \tag{1}$$

$$A = \frac{4\sigma_{s/a} M_w}{RT\rho_w} \quad (2)$$

with A composed of σ_s/a = 0.072 ~~J~~ $\mathrm{J\,m^{-2}}$ the surface tension of pure water, $\mathrm{M_w}$ = 0.018 ~~Kg~~ $\mathrm{kg\,mol^{-1}}$ the molecular weight of water, R = 8.314 ~~J~~ $\mathrm{J\,mol^{-1}\,K^{-1}}$ the perfect gas constant, T the activation temperature in K and ρ_w = 997 ~~kg~~ $\mathrm{kg\,m^{-3}}$ the density of water. $\mathrm{D_d}$ is the activation diameter in ~~nm~~ nm calculated for a given supersaturation $\mathrm{S_c}$. Note that hygroscopic particles have theoretical Kappa values between 0.5 and 1.4. Petters and Kreidenweis (2007) summarized several κ values derived from CCN measurements. κ values are 1.28 and 0.9 for ~~NaCl~~ NaCl and $\mathrm{H_2SO_4}$ respectively. When the $\mathrm{Na^+}$ ion is associated with other compounds, its κ values decrease and range between 0.8 and 0.88. Ammonium sulfate has κ values between 0.61 and 0.67. Organic compounds have κ values between 0.01 and 0.4 and hydrophobic aerosols such as black carbon are 0.

4.3 Method of classification of air masses arriving along the Marion Dufresne path

Back-trajectories provide additional information to understand the origin of the air mass and thus help to better understand the observed aerosol size distribution and properties. For that, the ~~FLEXPART~~ FLEXible PARTicle Model (FLEXPART) version 10.4 (Pisso et al., 2019) has been used from the vessel's position.

The ~~FLEXible PARTicle~~ FLEXPART model is part of the multi-scale offline Lagrangian Particle Dispersion Models (LPDMs) which have been developed to simulate transport and turbulent mixing of aerosols and gasses in the atmosphere. The model can be run for forward or backward simulations. In backwards mode, the location where particles are released, called a "receptor," is defined within a longitude-latitude-altitude cell (Pisso et al., 2019). For this study, ERA-5 meteorological fields with a spatial resolution of ~~0.5° x 0.5°~~ 0.5° x 0.5° and time resolution of ~~1h~~ one hour were used as input. Five-day back trajectories were run each hour of campaign at the location of the vessel with a particle release between ~~200 and 250 m~~ 0 and 50 m of altitude. To analyze the dataset according to the air mass origin, the area covered by the vessel was divided in three subdomains related to the main types of air masses. The continental air masses were identified as such when the residence time over the area north of ~~40°~~ 40° S and west of ~~50°~~ 50° E was the greatest. Air masses were classified in the Subtropical Indian Ocean group when the residence time over the area east of ~~50°~~ 50° E and north of ~~40°~~ 40° S was the greatest. Thus, the Southern Indian Ocean air masses were identified as such when the residence time over the area south of ~~40°~~ 40° S was the greatest. This classification led to ~~15385~~ 15,385 receptors in the ~~Southern~~ southern Indian Ocean group (with spatial extension [~~20° S-60°~~ 20° S-60° S] [~~35° E to 80°~~ 35° E to 80° E]), ~~5495~~ 5,495 receptors in the ~~Subtropical~~ subtropical Indian Ocean group (with spatial extension [~~20° S-50°~~ 20° S-50° S] [~~55° E-80°~~ 55° E-80° E]), and ~~4048~~ 4,048 receptors in the ~~Continental~~ continental group (mostly located north of Madagascar and around Reunion ~~island~~Island). This classification also resulted in a mixed zone where all three types of air mass are present in the middle of the ~~Subtropical~~ subtropical Indian Ocean.

5 ~~Spatial and temporal variability of marine aerosols properties~~

4.1 ~~Aerosol number concentration~~

~~Three modes were determined according to the average number~~ This classification resulted in 6,273, 18,647, and 9,049 SMPS data points (0.02-0.35 µm), and 2,305, 13,727, and 5,554 OPC-N3 data points (0.41-5.85 µm) used in the calculation of the average aerosol size distribution of the ~~filtered database derived from SMPS and OPC-N3 measurements: an Aitken and an Accumulation mode composed of sub-micron particles from 30 nm to 70 nm and from 71 nm to~~ continental, southern Indian Ocean, and subtropical Indian Ocean air masses, respectively.

5 Spatial and temporal variability of marine aerosols properties

Aerosol number concentration (N_{SMPS}) was calculated by summing the SMPS diameters ranging from 3 nm to 350 ~~nm (dry diameters) respectively, and a coarse mode made of super-micron particles of sizes ranging from 1.15 to 3.5 .~~ nm. Figure 4 shows the spatial variation of ~~total number concentration Na~~ N_{SMPS} (a), ~~of the Aitken mode (~~the cloud condensation nuclei concentration at 0.4 % SS (N_{CCN}) (b), ~~of the accumulation (c) and of the coarse mode (~~the activation diameter (D_{act}) at 0.4 % SS (c), and the Kappa-Köhler parameter (κ) at 0.4 % SS (d) along the vessel track during the six campaigns.

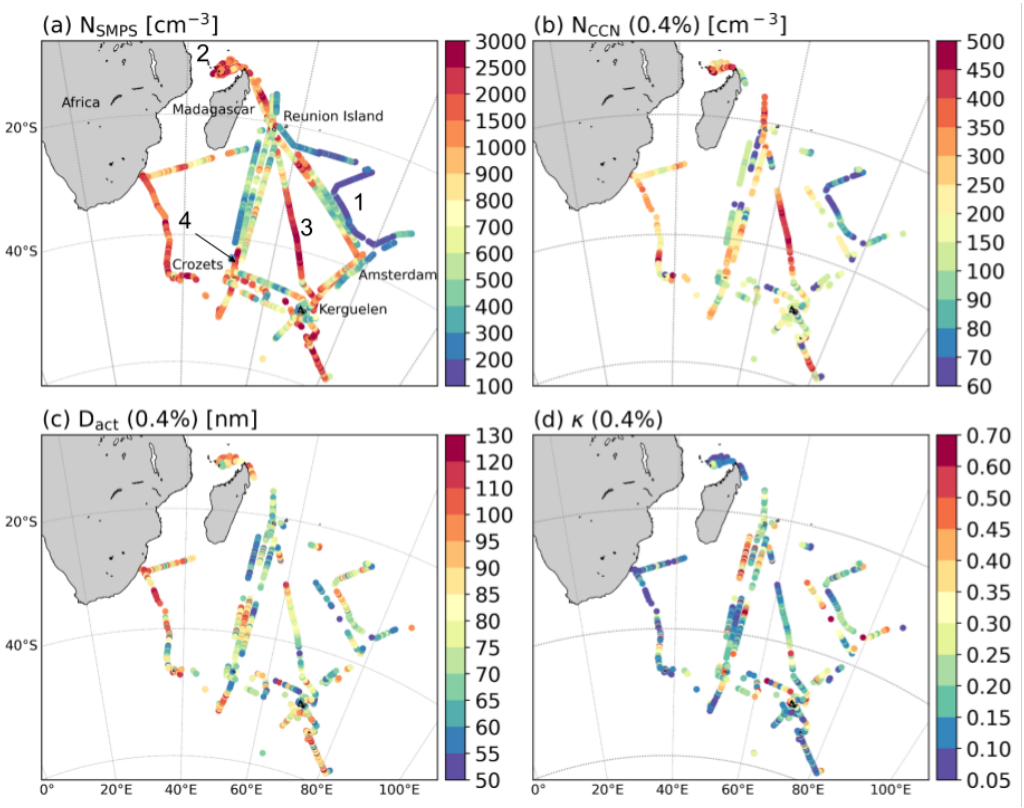

Figure 4. (a) Evolution of ~~the total number concentration of aerosols~~ (N_{SMPS}) measured by the SMPS from ~~30 nm~~ 3 nm to 350 ~~nm~~nm, (b) ~~in the Aitken mode (30 nm – 70 nm)~~N_{CCN} at 0.4 % SS, (c) ~~in the accumulation mode (71 nm – 350 nm)~~D_{act} at 0.4 % SS , (d) and ~~by the OPC-N3 in the coarse mode (1.15 – 3.5)~~ κ at 0.4 % SS along the path of the Marion Dufresne in 2021 and 2023.

~~Na~~ N_{SMPS} is highly variable on the sampling area with one order of magnitude between low and high concentrations~~(98~~ . The average N_{SMPS} is 1,149 $\pm$ 706 cm^{-3} (mean $\pm$ one standard deviation), with ~95 % of the values between 100 cm^{-3} and ~~2500~~ 3,000 cm^{-3}~~). In the Aitken mode, 97~~ . The average N_{CCN} at 0.4 % SS is 208 $\pm$ 102 cm^{-3}, with ~95 % of the ~~aerosol concentrations are between 50-1400~~ values between 60 and 500 cm^{-3}~~among which 10 % are smaller than 100 , and 14 % are greater than 800~~ . ~~In the accumulation mode (Fig. 4 (c)), 93 %~~ To further investigate the hygroscopic properties of the aerosol ~~concentrations are between 50-700 among which 17 % are between~~ population, the spatial variation of the activation diameter and κ were calculated according to Petters and Kreidenweis (2007) (Section 4.2). Activation diameters are highly variable (between 50 ~~and 100 and~~ - 130 nm) along the different routes taken by the Marion Dufresne, with an average value of 80 $\pm$ 15 ~~% are greater than 400 . In the coarse mode~~ nm (Fig. ~~4 (d)), 97~~ 4c). 98 % of the ~~aerosol concentrations are between~~ κ values are in the physical range between 0.05-0.7 at 0.4 % SS, with an average value of 0.2 $\pm$ 0.1 ~~- 8 within those less than 27 % are smaller than 0.5 and 10 % are greater than 3 . Sedimentation and below-cloud scavenging are efficient removal processes of large particles of diameters greater than 500 nm (Saltzman, 2009; Bae et al., 2012). Plus, the number of aerosols of diameters~~

~~greater than 500 nm produced by bubble bursting is very low at source (Monahan et al., 1986; Ovadnevaite et al., 2014; Sellegri et al., 2023~~ ~~. This explains why the aerosol number concentration is lower in this mode and decreases during transport. Thus, the highest aerosol number concentrations in this mode are observed in regions where primary production is more important, as it is the case south of 40 ° S during the three storms identified in Figure 2a.~~ (Fig. 4d). This indicates a large variability of the chemical composition and size distribution of aerosols in the southern Indian Ocean and the Southern Ocean.

The difference in the location of high and low aerosol concentrations reflects ~~distinct~~ different underlying processes. ~~Generally, an elevated concentration of submicron particles above oceans can be explained by (i) a gas-particle conversion process implicating the homogeneous nucleation of sulfuric acid (Kulmala et al., 1998),~~ N_{SMPS} less than 200 cm^{-3} (Fig. 4a; label 1) are mostly observed in the eastern part of the Indian Ocean [20° S-40° S; 60° E-80° E] during OBSAUSTRAL. In this region, 90 % of N_{SMPS} is less than 300 cm^{-3} and shows low variability. These low concentrations are explained by the observed weak to moderate wind speed (< 10 $m\,s^{-1}$) ~~(ii) by primary emission from bubble bursting (Clarke et al., 2003), (iii) by an entrainment of nanoparticles from the free troposphere (Zheng et al., 2021), or (iv)by advection of polluted air mass from the continent (Wang et al., 2020).~~ Fig. 2a) and by the area being far from any continent. Similarly, N_{CCN} is generally less than 70 cm^{-3}, which corresponds to the lowest concentrations observed across all campaigns (Fig. 4b).

~~Na greater than 1000~~ N_{SMPS} greater than 1,000 cm^{-3} are mostly observed north of Madagascar (Fig. ~~4 (a), label 1a~~4a; label 2). In this area [~~0° S-20° S; 40° E-50°~~ 0° S-20° S; 40° E-50° E] only 7 % of the data have ~~Na~~ N_{SMPS} below 500 cm^{-3}. ~~The Aitken mode largely contributes to these high Na values and accounts on average for 61 % of Na.~~ High concentrations of CO, ~~CO2, CH4, and O3~~ CO_2, CH_4, and O_3 were also observed (Tulet et al., 2024), suggesting a continental influence in these areas. ~~These results are in-line with polluted air masses observed over the Atlantic Ocean during the Tara Pacific Expedition (Flores et al., 2020). Koponen et al. (2002) also reported a number concentration of aerosols greater than 2000~~ This region is also associated with an average N_{CCN} of 271 ± 86 cm^{-3}~~related to air masses coming directly from Europe during a cruise between the English Channel and the coast of Antarctica~~. The activation diameters are generally greater than 80 nm (Fig. 4c), and the associated κ drops to values between 0.05 and 0.15, corresponding to aerosols mostly hydrophobic.

~~Na concentration between 800-1000~~

A high N_{SMPS} value, between 900 and 3,000 cm^{-3}~~are observed off the southeast coast of Africa~~ , is also observed along the transects where the Marion Dufresne encountered storms during SWINGS (Fig. ~~4 (a), label 1b), but are not related to continental air masses as suggested by the 5-day back trajectories calculation, and are rather related to air masses coming from south of 40° S.~~ 2a; black circles). However, as it is clearly visible along the transect between the Kerguelen Islands and Reunion Island, this high N_{SMPS} concentration is not limited to the wind speed peaks (south of 40° S) and extends further north (Fig. 4a; label 3). Along this transect, ~~the percentage of aerosols in the free troposphere is higher than the one in the marine boundary layer 2 days before the air masses arrive at the ship's location. This suggests an intrusion of free-tropospheric air masses into the marine boundary layer.~~

~~Peaks of Na concentration are also visible east of Prince Edward islands~~ N_{CCN} varies similarly to N_{SMPS}, with concentration between 250 and 500 cm^{-3}. The activation diameter increases from 50 to 120 nm as the vessel approaches Reunion Island. The κ values are first between 0.2 and 0.5 in the maximum wind speed region, then gradually decrease from 0.6 to 0.2 between

40°S and Reunion Island (Fig. ~~4 (a), label 1c). Available measurements of Aerosol Optical Depth (AOD) over the period is between 0.141 and 0.893 (, last access: 19 November 2024). According to Mallet et al. (2018), AOD values greater than~~ 4d). Another period is marked by a sharp increase in N_{SMPS} from 400 to more than 3,000 cm^{-3} between 35° S and the Crozet Islands during OP3 (Fig. 4a; label 4). However, along this transect, N_{CCN} (200 - 350 cm^{-3}) does not follow the increase in N_{SMPS} and changes little. It is also observed that the activation diameter (70 - 90 nm) and κ (0.1 - 0.2) vary little, suggesting that the increase in N_{SMPS} comes from particles smaller than the activation diameter.

To explain this variation of N_{SMPS} in the ~~Indian Ocean indicate that the air mass has a continental origin and comes from South Africa or Australia. This hypothesis is likely as the air mass is located above the marine boundary layer the day before it reaches the ship's location.~~ region, the four situations presented in the present section are discussed below.

~~Na smaller than~~

6 Focus on particular events

Among the numerous situations observed during the 6 campaigns presented in this paper, several deserve to be detailed in order to analyze their origins or specific processes. Four types of situations (Fig. 5) have been selected which led to N_{SMPS} observations smaller than 200 ~~(Fig. 4 (a)~~ cm^{-3} or peaks above 3,~~label 2) are mostly observed in the eastern part of the Indian Ocean~~ 000 cm^{-3}.

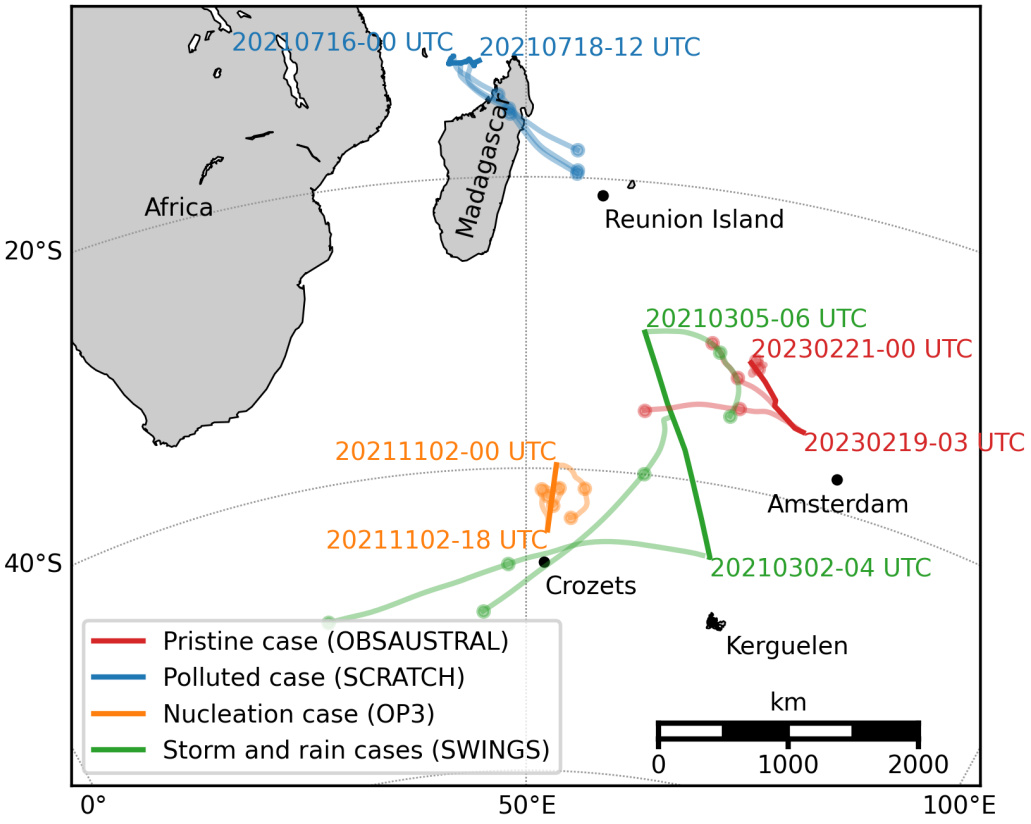

Figure 5. Position of the Marion Dufresne (thick lines) and 2-day back-trajectories (thin lines) from the FLEXPART model for the four selected situations, illustrating the origins of the air masses (1 dot per day).

6.1 Pristine case (OBSAUSTRAL)

A case of pristine air mass observed on February 19 and 20~~° S-40° S; 60° E-80° E during OBSAUSTRAL. This region is associated with weak to moderate wind speed (< 10 m) (Fig. 2a) and is far from any continental influence as the 5-day back trajectory air masses came from the Southern Indian Ocean (example in Fig. 11). In this region, 90 % of Na is smaller than 300 and exhibit low variations. Aerosol number concentration in the Aitken and accumulation modes is mostly lower than 160 and shows weak variations in the Aitken mode. The coarse mode~~ , 2023 is shown in Figure 6 and is associated with ~~weak concentrations lower than~~ the low N_{SMPS} observed along the easternmost transect of OBSAUSTRAL (Fig. 4a; label 1~~with most values between 0.1 and 0.6 . These features suggest that~~). During this period, the air masses arriving at the ~~vessel may have aged, and that there were no significant sources of new particles. Another possibility is~~ ship's position evolved over the subtropical Indian Ocean, far from the continents. The height of the backtrajectory shows that the air mass ~~may have experienced low wind speed or wash out.~~

~~During the three storms of SWINGS~~ remained in the oceanic boundary layer, i.e. below 1,000 m, for the three days prior to the measurement (Fig. ~~2 (a), black circles), Na is between 700-1000 (Fig. 4 (a), label 3a, 3b and 3c~~6a to 6d). During this period, the aerosol size distribution is very stable, with a clearly visible Aitken mode around 50 nm and a weak and broad accumulation mode between 150 and 300 nm. This large accumulation mode mean diameter and the lack of mode evolution indicate that the air mass is aged (Fig. 6e). ~~The transects 3a and 3b are associated with the highest concentrations of aerosols in the coarse mode (5.56 $\pm$ 4.48 N_{SMPS} and N_{CCN} remained low, between 150 - 250 cm^{-3} and 4.58 $\pm$ 3.70~~ 40 - 120 cm^{-3}~~) compared with the transect 3b (1.85 $\pm$ 2.65). Plus, over the period of high wind speed (> 10 m), the average ratio of~~ , respectively (Fig. 6f). Throughout the day, the activation diameter is between 60 and 140 nm and lies between the Aitken mode ~~concentration to~~ and the accumulation mode~~concentration is the highest along the transect 3b (1.93 $\pm$ 0.88), compared with the values along the transects 3a and 3b (1.12 $\pm$ 0.37 and 1.1 $\pm$ 0.31). In their study, Koponen et al. (2002) catched several episodes of high number concentration of aerosols (close or above 1000) between Cape Town, South Africa, and 55° S, which were due to elevated concentrations in the Aitken mode, whereas between 55-60 ° S the high number concentration of aerosols were due to elevated concentrations in the nucleation mode. More recently, McCoy et al. (2021) described an aerosol mechanism occurring in the Southern Ocean which explains the high concentrations of Aitken mode particles in the marine boundary layer. This mechanism is triggered by emissions of dimethyl sulfide (DMS), which is uplifted by synoptic scale motions into the free troposphere. There, new particles can be formed by nucleation of DMS oxidation products (mainly sulfuric acid), which constitute a reservoir of small aerosols above clouds. When free tropospheric air masses subside into the marine boundary layer, these small aerosols grow into CCN sizes via gas condensation and cloud processing and impact cloud droplet number.~~ , in a very low concentration zone close to the measurement noise. The κ values obtained range from 0.1 to 0.5 at 0.2% SS and from 0.1 to 0.3 at 0.4% SS. Specifically, when N_{SMPS} and N_{CCN} concentrations are exceptionally low, it has been observed to induce a decrease in κ. This decrease occurs without any discernible pattern in the particle size distribution or in the origin of the air mass. This situation illustrates a case where the calculation of κ based on the combination of two instruments exhibits an important sensitivity to low concentrations. Consequently, the resultant value should be considered with caution.

6.2 ~~Cloud condensation nuclei concentration~~

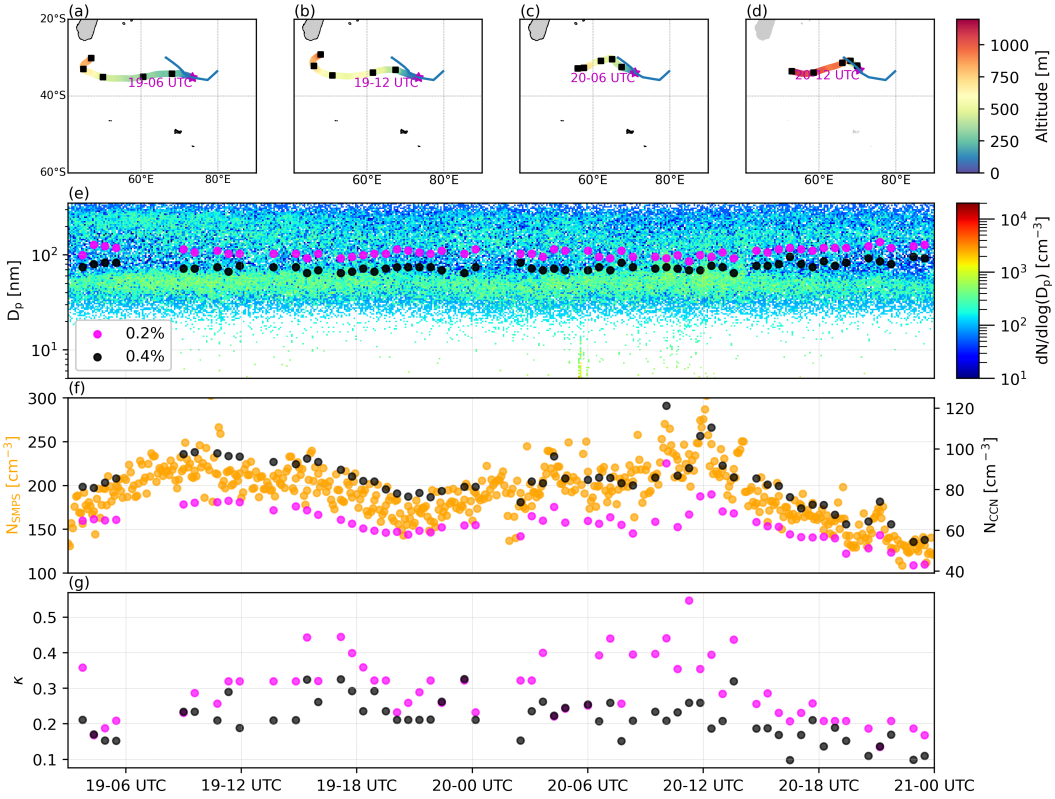

Figure 6. ~~Evolution~~ (a), (b) (c) and (d) 10 m wind speed from ERA5 along 3 FLEXPART back-trajectories at four instant. Blue contours correspond to areas where rain rate is higher than 0.1 mm h^{-1} at that instant. (e) Temporal evolution of ~~the number of~~ aerosol size distribution and activation diameter, (f) aerosol concentration (N_{SMPS}) and cloud condensation nuclei (N_{CCN}) at 0.2 and 0.4 % supersaturation, and (~~a~~g) hygroscopicity parameter (κ) at 0.2 and 0.4 % ~~(b)~~ supersaturation ~~along~~ observed on February 19 and 20, 2023 during the ~~path of the Marion Dufresne~~OBSAUSTRAL campaign (Fig. 1).

~~When it comes to discussing the activation properties of aerosols we use the term Condensation Nuclei (CN). CN is equivalent to Na used previously and represents the total aerosols number concentration. Cloud Condensation Nuclei (CCN) refers to the subset of CN on which the atmospheric water vapor condenses upon at a given supersaturation (SS) to form cloud droplets. Thus CCN/CN gives the proportion of potential cloud droplets among the aerosol population. The variation of this ratio can be explained by a variation in the aerosol chemical composition and size distribution.~~

~~Fig. 5 shows the spatial variation of CCN concentration at 0.2 % and 0.4 % SS. 95 % of CCN number concentration is between 40 and 500 at both SS. The average CCN concentration is 161.1 ± 82~~

6.2 Polluted case (SCRATCH)

Figure 7 shows the evolution of the aerosol particle size distribution (e), N_{SMPS} and CO concentrations (f) between July 16 and ~~190.5 ± 102.5 (mean ± one standard deviation)~~ 19, 2021. The origin of the air mass is also represented by the height of the back trajectory over the period (Fig. 7a to 7d). During this period, CO and N_{SMPS} concentrations remained high (> 50 ppb and > 2,000 cm^{-3}, respectively), showing that the area was generally affected by residual continental pollution. The activation diameter remained high (~ 128 nm at 0.2 % SS and ~ 92 nm at 0.4 % SS~~. These results are in the range of CCN concentrations reported by Sanchez et al. (2021) between Tasmania and Antarctica (45° S-70° S),where CCN concentrations are between~~ ~~50-150~~ ~~)~~ and κ values were less than 0.19. Several peaks of N_{SMPS} > 6,000 cm^{-3} ~~at 0.2 % SS, and between 90-230 at 0.4 % SS, regardless of the cloud processes affecting the air masses they analyzed.~~

~~Region 1a is~~ were also measured periodically and are associated with a significant increase in CO concentrations of 10 to 15 ppb, indicating that the air mass was affected by anthropogenic pollution. The aerosol size distribution shows that these N_{SMPS} peaks are associated with an ~~average CCN concentration of 261.9 ± 188.4 and 426.3 ± 255.5 at 0.2 % and 0.4 % SS, respectively. Along the transect 2, CCN concentration is mostly lower than 50~~ increase in the number of aerosols in the Aitken mode ~~(100) at 0.2 % SS (0.4 % SS). Such a low concentration in this area is not surprising since the aerosol number concentration in the accumulation mode , which contributes significantly to the CCN concentration, is already low (Fig. 4 (c)). In their study, Sanchez et al. (2021) attributed low Na and CCN concentration events to scavenging. Their measurements exhibit CCN concentrations lower than 100 at 0.2 % and 0.4 % SS, and the lower CCN concentration at 0.3 % SS corresponded to the highest total precipitation.~~

~~Between 40-45 ° S and 45-50 ° S, the latitudinal distribution of CCN at 0.2 % SS (189.4 , 128.5) is similar to the one obtained by Humphries et al. (2021) (169~~ 30 to 40 nm) and the appearance of a new nanoparticle mode located between 5 and 30 nm. The backtrajectory analysis clearly shows the passage of the air mass at about 800 m a.g.l. over the urbanized region of Majunga, northwest Madagascar. The temporal evolution of the mixing boundary layer (MBL) thickness over Madagascar, corrected for transport time, is shown in Figure 7g. There is a clear correlation between the MBL thickness and the CO and N_{SMPS} peaks: each concentration peak is associated with an MBL thickness greater than 800 m. This means that only the upper part of the polluted boundary layer over Madagascar can reach the ship by subsidence. This can only happen in the afternoon when the boundary layer is sufficiently developed. This situation shows that the high variability in aerosol concentration between 800 and 8,~~131) . Between 50-55 ° S and 55-60 ° S, the CCN concentrations (169.2~~ 000 cm^{-3} ~~, 185.1) are higher than the one obtained by Humphries et al. (2021) (102 in both latitudes range). This difference in the high latitudes range is certainly due to the low number of data collected in this area during MAP-IO.~~

~~Along the transects 3~~ observed in the northern Mozambique Channel (Fig. ~~5; label 3a, 3b, 3c) , CCN concentration at 0.2 % SS is relatively similar. However,~~ 4a; label 2) can be explained by a residual polluted air mass that evolves with the diurnal evolution of the MBL over Madagascar. This important aerosol number has low impact on N_{CCN}. Moderate N_{CCN} observed are ranging from 100 to 500 cm^{-3}, and are attributed to elevated activation diameter values (> 100 nm) that exceed the residual continental pollution mode. The resulting κ is low, ranging from 0.06 to 0.1 at 0.4% SS ~~, CCN concentration is higher~~

~~for transect 3b (299 ± 131) and 3c (305 ± 134), compared with the one for transect 3a (223 ± 94). These transects are also marked by the development of an accumulation mode following the maximum wind speed, which allows CCN concentration to increase~~and from 0.1 to 0.2 at 0.2% SS. This indicates an air mass composed primarily of hydrophobic aerosols.

6.3 ~~Activation diameters and hygroscopicity~~

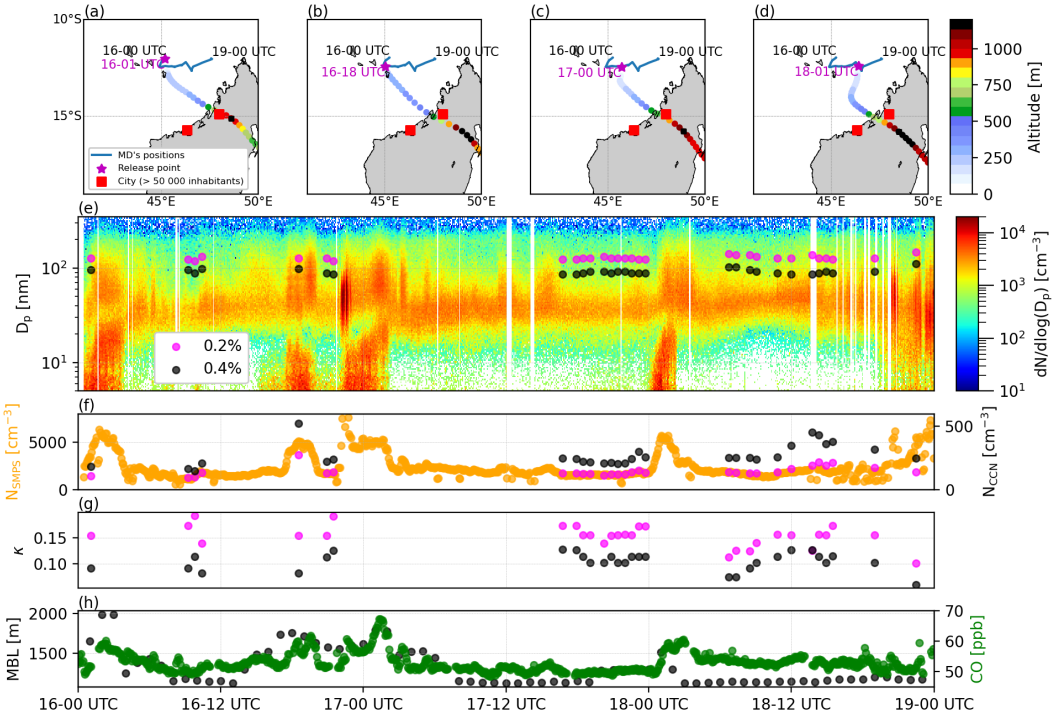

Figure 7. ~~Evolution~~ (e) Temporal evolution of ~~the~~ aerosol size distribution and activation ~~diameters~~ diameter, (~~a~~f) ~~,~~ aerosol number concentration (~~b~~N_{SMPS}) ~~)~~ and ~~kappa parameter~~ cloud condensation nuclei concentration (~~c~~N_{CCN}) observed from July 16 to 19, 2021 (~~d~~SCRATCH campaign, Fig. 1). (g) aerosol hygroscopicity (κ) at 0.2 ~~%~~ and 0.4 % ~~supersaturation~~ SS. (h) CO concentration at the Marion Dufresne location, and mixing boundary layer (MBL) thickness evolution during 3 first hours over West of Madagascar along FLEXPART back-trajectories. (a : 16-00 UTC, b : 16-18 UTC, c : 17-00 UTC, d : 18-01 UTC) Altitude of air masses along FLEXPART back-trajectories for the ~~path~~ four CO peaks. The red squares correspond to the locations of the ~~Marion Dufresne~~most urbanized areas in Majunga province (Madagascar).

~~To further investigate the hygroscopic properties of the aerosol population, the spatial variation of the activation diameter and κ have been computed according to Petters and Kreidenweis (2007) (section 3.2). Fig.~~

6.3 Storm and rain cases (SWINGS)

The third period highlighted corresponds to a case of primary aerosol emission observed during the SWINGS campaign between March 2 at 00 UTC and March 6 ~~presents the activation diameters (Fig. 6a and c)) and the corresponding~~ at 00 UTC 2021. Three periods can be identified. On March 2, prior to 06 UTC, the air mass moved from the west into a storm zone and is characterized by ERA5 winds that exceeded 18 $\mathrm{m\,s^{-1}}$ (Fig. 8a). The vessel was affected by this storm, with measured swells exceeding 14 m and wind speeds reaching 25 $\mathrm{m\,s^{-1}}$. The air mass was also under the influence of rain, which limited the aerosol concentration due to washout, particularly prior to 03 UTC ($\sim$ 500 $\mathrm{cm^{-3}}$) (Fig. 8a, d, e). The activation diameter was observed to range between 60 and 100 nm, with significant fluctuations in hygroscopicity, as indicated by variations in κ, ranging from 0.2 to 1 (Fig. ~~6b and d)~~8f). During the second period, from March 2 at 18 UTC to March 3 at ~~0.2 (top panel) and 0.4 % SS (bottom panel). Activation diameters and κ are highly variable along the different routes taken by the Marion Dufresne indicating a large variability of the chemical composition and size distribution of aerosols in the Southern Indian Ocean and the Southern Ocean. Globally lower κ are observed when SS increases. 97 % of the κ values are in the physical range between 0.05-1.2 at both SS, with an average value of 0.36 $\pm$ 0.2~~ 06 UTC, a decline in wind and wave height conditions was recorded (Fig. 8b, g). On March 2 at 18 UTC, the ship moved approximately 300 km northwestward. The measured wind and wave height remained elevated, and the air mass continued to be exposed to strong winds exceeding 20 $\mathrm{m\,s^{-1}}$ over the past 24 hours. According to the ERA5 analyses, this air mass was not affected by rain. This explains why the aerosol concentrations measured on the Marion Dufresne exceeded 3000 $\mathrm{cm^{-3}}$ despite the slight decrease in wave height and wind intensity. Aerosol hygroscopicity increased overall but remained variable, with a kappa ranging from 0.2 ~~% SS~~ to 1 (Fig. ~~6 (b)), and 0.25 $\pm$ 0.18 at 0.4 % SS (Fig. 6 (d)). The percentage of κ values greater than 1 are negligible (1.5 % at 0.2 % SS and 0.9 % at 0.4 % SS). The average activation diameter is 104.1 $\pm$ 19.7 nm at 0.2 % SS (Fig. 6a),and 76 $\pm$ 16.3 nm at 0.4 % SS~~ 8g). The third period begins at 06 UTC on March 3. SMPS data show the persistence of a pronounced Aitken mode around 30 nm and a concentration of approximately 2,000 $\mathrm{cm^{-3}}$ (Fig. ~~6c).~~

~~Higher activation diameters are observednorth of Madagascar at both SS (Fig. 6 (a); label 1a). The associated κ falls down to values between 0.05-0.2 at 0.4 % SS, corresponding to hydrophobic aerosols. This result corresponds to the most polluted air mass due to the proximity of continental emissions as mentioned before.~~

~~High activation diameters (> 110 nm) are also observed along the transect 2~~ 8d, e). The formation of a second mode is also observed, whose size increases over the period and reaches a size characteristic of the accumulation mode around 100 nm. During this period, the Marion Dufresne maintained a course northwestward, away from the storm center. According to the ERA5 data, on March 3 at 18 UTC, the air mass remained unimpacted by rain and had experienced moderate winds of approximately 10 $\mathrm{m\,s^{-1}}$ the previous day (Fig. ~~6(a)) at 0.2 % SS, which is in line with the previous observations of Na and CCN (Section 4.1 and 4.2)in this region.~~

~~During the storm events (Fig. 6; label 3a, 3b, 3c)~~ (8c). Observations from the Marion Dufresne indicate that the sea remained rough until at least 06 UTC on March 4, with wave heights ranging between 6 and 10 m (Fig. ~~1), a significant drop in~~ 8g). Although the total aerosol concentration remained largely stable during this period, it is noteworthy that as the air mass aged, an accumulation mode emerged (probably through coagulation processes), resulting in a continuous decline in the κ ~~values is observed between~~ from 0.7 on March 3 at 06 UTC to 0.2 ~~% SS and 0.4 % SS associated with primary emission. The average κ~~

~~calculated over a one-day storm is 0.35, 0.41, and 0.53~~ on March 5 at 00 UTC (Fig. ~~6 (b); label 3a~~8f). As a partial conclusion, the findings indicate that the aerosol concentration is determined by the equilibrium between various factors, including advection, local primary production and loss through precipitation. It is important to note that the maximum concentration of aerosols is not necessarily attained during periods of peak wind speed and wave height.

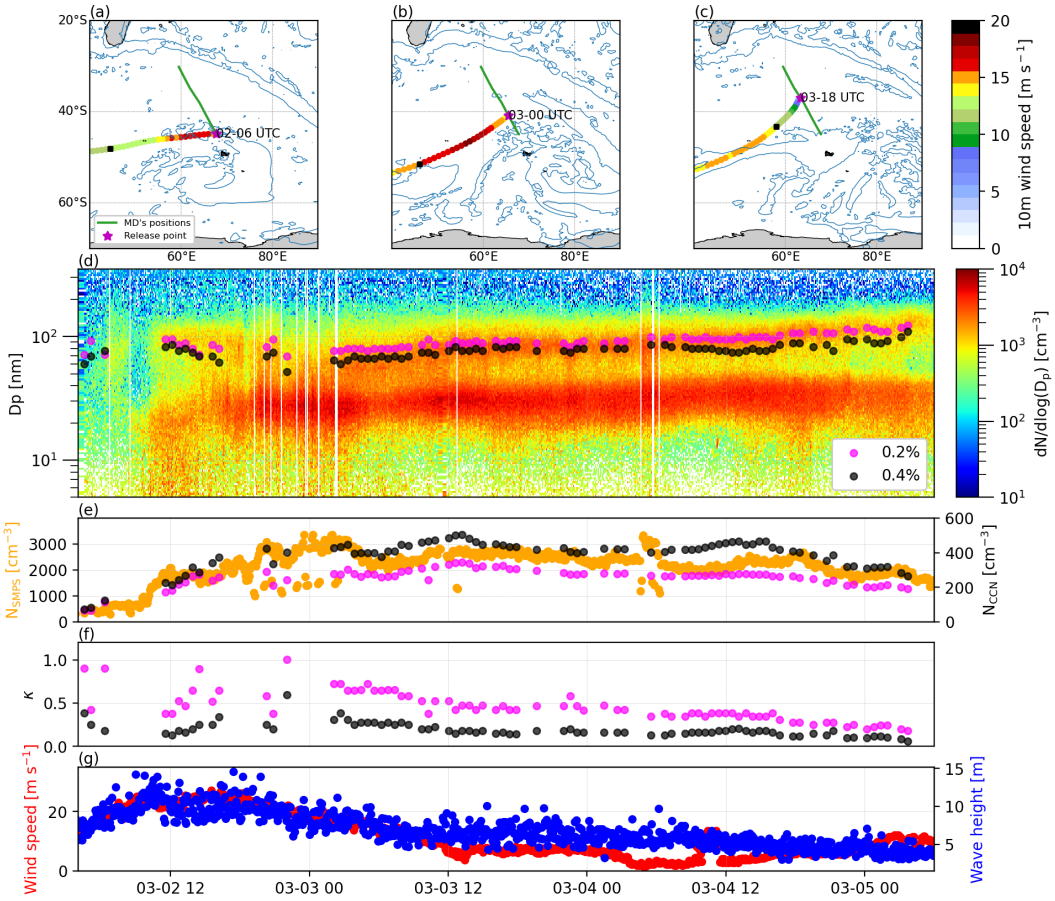

Figure 8. (a), (b) and (c) 10 m wind speed from ERA5 along 3 FLEXPART back-trajectories at three instant. Blue contours correspond to areas where rain rate is higher than 0.1 $\mathrm{mm\,h^{-1}}$ at that instant. (d) Temporal evolution of aerosol size distribution and activation diameter, (e) aerosol concentration and cloud condensation nuclei at 0.2 and 0.4 % SS. (f) hygroscopicity parameters at 0.2 and 0.4 % SS. (g) wind speed and wave height observed from March 2 to 5, 2021 during SWINGS campaign (Fig. 1).

6.4 Nucleation case (OP3)

Figure 9 shows the evolution of aerosol concentration (N_{SMPS}, N_{CCN} and size distribution) and ship tracks superimposed on a cloud mask based on satellite brightness temperature (cloud areas correspond to brightness temperatures below 282 K; (e.g., Janowiak et al., 2017a; Wang et al., 2017)) on September 11, 2021. The satellite images in Figure 11 show that the ship

was in a cloudy area until 07 UTC (11 LT), then passed through a clear sky area between 09 UTC and 15 UTC, before returning to a cloudy area. Before 08 UTC (∼12 LT), ~~3b, 3c) at 0.2 % SS. At 0.4 % SS, this value is 0.2, 0.19, and 0.23. The average κ~~ SMPS measurements clearly show two modes at 30 nm and 130 nm associated with a N_{SMPS} of 500 cm^{-3}. The measured N_{CCN} is low: 178 cm^{-3} at ~~0.4 % SS (Fig. 6 (d)) falls in the range of κ values of organic matter (0.1-0.2) according to Petters and Kreidenweis (2007). Hence, here the presence of organic matter could explain this decrease in the hygroscopicity, with a more visible effect on smaller aerosols (O'Dowd et al., 2004).~~

~~On the other hand, more hygroscopic species are observed along the transects between Reunion island and the Crozet islands (Fig. 6(b); label 4) during OP4, OBSAUSTRAL, and between Kerguelen islands and Amsterdam island during OP4 (Fig. 1). The average κ is 0.8 ± 0.3 at~~ 0.2% SS and ~~0.6 ± 0.3~~ 221 cm^{-3} at 0.4% SS. The ~~activation diameter is already low at 0.2 % (70-90 nm) and κ values are relatively high, mostly between 0.6 and 1. Here, the aerosol population seems to consist of both sulfates and organic species generated either by the local environmental conditions or transported from farther sources. Hence, over these periods, the wind speed is globally between 10-20 m , and the ship is influenced by air masses located above the marine boundary layer before arriving at its location.~~

~~Along the transect 5, high κ values are observed at both SS, while the activation diameter decreases from 70 to 40 nm. During this period, the wind speed is between 5-17 m , the wave height is between 4-8 m, and the number concentration of aerosols in the coarse mode~~is between ~~0.7-1 . Plus, the air mass stayed in the marine boundary layer. Here, the local weather conditions led to the emission of primary marine aerosols constituted of inorganic species.~~

~~Between Kerguelen islands and Amsterdam island during OBSAUSTRAL (Fig. 6 (c); label 6), low κ values (0.1-0.2) are observed at both SS~~0.1 and 0.4. A sharp increase in N_{SMPS} is observed at 9 UTC, reaching 4~~,and do not vary much from 0.2 % to~~ 000 cm^{-3} at 13 UTC. The SMPS size distribution depicts the formation of new particles at 9 UTC (5 nm), which is associated with a classic banana-shaped growth (condensation-coagulation) that is characteristic of nucleation events (Kulmala and Kerminen, 2008; Foucart et al., 2018; Määttänen et al., 2018, and references cited). In addition, the formation of new particles is concomitant with the transition from cloudy to clear skies. The activation diameters at 0.2 and 0.4% SS are larger than the size of the nucleation mode. During the nucleation process, the Aitken mode demonstrates growth from 30 nm to 80 nm, which exceeds the activation diameter at 0.4% SS. Thus, the N_{CCN} at 0.4% SS ~~. The air mass originated from Antarctica. Along this transect, Na decreases from 500~~ increases from 220 cm^{-3} ~~to 250~~ (08 UTC) to 350 cm^{-3} (~~Fig. 4a)and on the SMPS scan, the accumulation mode moves towards larger diameters with its lower diameter increasing from 100 nm to 200 nm. Thus this transect is a typical case of aerosol aging over time. The decrease in sea spray aerosols hygroscopicity due to aging has been widely studied and is discussed in Su et al. (2022). The authors focused on chloride depletion through air mass transport, generally observed when air masses originated from the continent. The magnitude of the chloride depletion increases following the order land-coastal area-remote ocean. Heterogeneous reactions between sea spray aerosols and atmospheric oxidants (e.g., O3, OH) and acidic species (e.g., nitrogen and sulfur organic species, organic acids) have been identified as playing a key role in chloride depletion during atmospheric transport.~~

~~At~~ 10 UTC), while the N_{CCN} at 0.2~~% SS, the median (0.38) and interquartile values (0.26 and 0.52 for 25th and 75th quartiles) of~~ % SS remains relatively stable throughout the day. The κ ~~between 40-60° S are in good agreement with the results~~

~~found in Tatzelt et al. (2022), in which the median value is ~0.4, and the 25th and 75th quartiles are ~0.3 and ~0.65. Between 45-60° S, the 5° latitude bin averaged κ values at 0.2 % SS (0.4 % SS) range between 0.38-0.5 (0.1-0.2). In comparison, in Sanchez et al. (2021), these values globally range between 0.1-0.5~~ at ~~0.3 % SS, independently of the atmospheric processes affecting marine aerosols.~~ 0.4% of SS increases at 0.46. This increase in hygroscopicity is likely associated with the condensation of semivolatile oxidized species on the Aitken mode, which undergoes a simultaneous evolution from a median diameter of 50 to 90 nm. This nucleation situation observed during OP3 (Fig. 4a; label 4) demonstrates the possibility of a rapid increase in the number of marine aerosols in pristine areas without being associated with strong increases in CCN concentration.

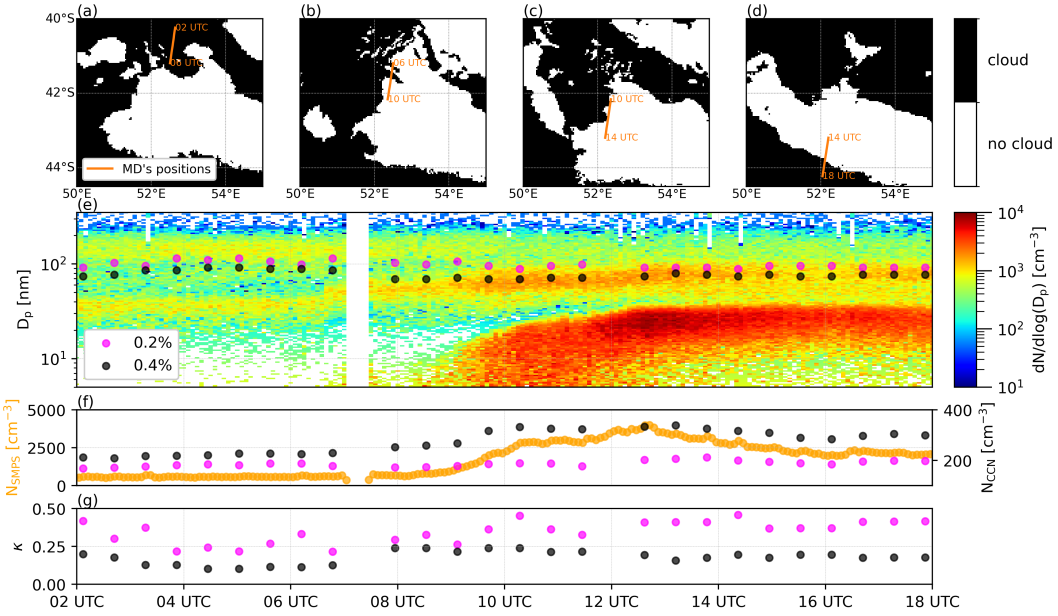

Figure 9. (a, 02-06 UTC), (b, 06-10 UTC), (c, 10-14 UTC) and (d, 14-18 UTC) Cloud cover and Marion Dufresne positions. (e) Temporal evolution of aerosol size distribution and activation diameter at 0.2 and 0.4 % SS. (f) aerosol concentration and cloud condensation nuclei at 0.2 and 0.4 % SS. (g) hygroscopicity at 0.2 and 0.4 % SS observed on November 2, 2021 (OP3 campaign, Fig. 1).

595 **7 Aerosols size distribution based on their air mass origin**

7.1 Size distribution of marine aerosols

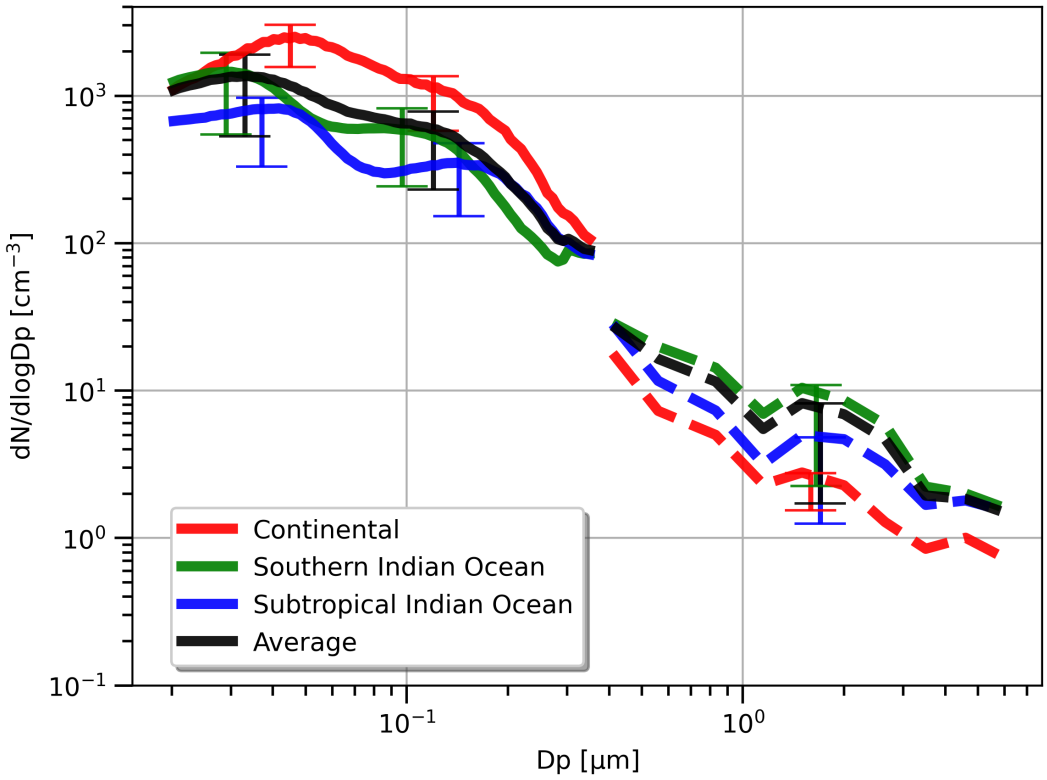

Figure 10. Average size distributions of aerosols according to air mass origin (continental, ~~Southern~~ southern Indian Ocean or ~~Subtropical~~ subtropical Indian Ocean) of the 5-days back-trajectories simulated by the FLEXPART model. Solid lines are average size distributions derived from SMPS data and dashed lines are average size distributions derived from OPC-N3 data. Bottom and top limits of error bars centered in the mean geometric diameter of each mode are the ~~25th~~ 25th and ~~the 75th~~ 75th quartiles.

	Continental	Southern Indian Ocean	Subtropical Indian Ocean	Average
Aitken mode	D = 45 nm	D = 29 nm	D = 37 nm	D = 33 nm
	σ = 1.52	σ = 1.5	σ = 1.54	σ = 1.73
	N= 1100 cm^{-3}	N = 650 cm^{-3}	N = 400 cm^{-3}	N = 830 cm^{-3}
	RMSE = 19.2 cm^{-3}	RMSE = 13.9 cm^{-3}	RMSE = 10.2 cm^{-3}	RMSE = 15.1 cm^{-3}
Accumulation mode	D = 120 nm	D = 97 nm	D = 143 nm	D = 120 nm
	σ = 1.56	σ = 1.56	σ = 1.52	σ = 1.52
	N= 490 cm^{-3}	N = 285 cm^{-3}	N = 160 cm^{-3}	N = 240 cm^{-3}
	RMSE = 16.9 cm^{-3}	RMSE = 10.5 cm^{-3}	RMSE = 6.7 cm^{-3}	RMSE = 12.4 cm^{-3}
Coarse mode	D = 1.59 µm	D = 1.65 µm	D = 1.7 µm	D = 1.7 µm
	σ = 1.53	σ = 1.56	σ = 1.5	σ = 1.5
	N= 1.17 cm^{-3}	N = 4.5 cm^{-3}	N = 2.2 cm^{-3}	N = 3.3 cm^{-3}
	RMSE = 0.5 cm^{-3}	RMSE = 1.05 cm^{-3}	RMSE = 0.69 cm^{-3}	RMSE = 0.93 cm^{-3}

Table 2. Geometric parameters of each mode of aerosol average size distributions (mean diameter, log-normal standard deviation and total number concentration).

~~Figure 7~~

Figure 10 shows the average aerosol size distributions as a function of air mass origin ~~,~~calculated by FLEXPART using the method described in ~~section 3.3~~Section 4.3. Table 2 presents the corresponding geometric parameters ~~of~~ for each mode fitted ~~on~~ to a log-normal distribution. ~~For the SMPS data (0.02-0.35) 6273, 18647, and 9049 data were used in the calculation of the average aerosol size distribution of the continental, Southern Indian Ocean, and Subtropical Indian Ocean air masses. For the OPC-N3 data (0.41-5.85), 2305, 13727, and 5554 data were used in the calculation of the average size distribution of the continental, Southern Indian Ocean, and Subtropical Indian Ocean group. Independently of the origin of air masses, three modesare visible in the size distribution. The average~~ Regardless of the origin of the air mass, we can highlight the Aitken, Accumulation, and Coarse modes. The mean diameters of the Aitken, accumulation, and coarse modes are 33 ~~nm~~nm, 120 ~~nm~~nm, and 1.7 µm, respectively, and the standard deviations are 1.73, 1.52, and 1.5. ~~Two other modes were also detected between 300 nm and 1 but are not considered in the discussion as their position is in the upper limit detection of the SMPS and the lower limit detection of the OPC-N3 respectively. The differences in the coarse modeare more visible in the number concentration of aerosols rather than the mean diameters and standard deviation. The continental, Subtropical Indian Ocean , and Southern Indian Ocean air masses exhibit a number concentration of aerosols of 1.17,~~

For the coarse mode, the mean aerosol number concentration is highest for air masses originating in the southern Indian Ocean (4.5 ~~, and 2.2~~ cm^{-3}~~(average number concentration of 3.3) with a mean diameter of 1.59, 1.65, and 1.7 (average position at~~

~~1.7). The number concentration of aerosols is the greatest for the Southern Indian Ocean air masses and the lowest for the~~) and lowest for continental air masses ~~, consistent with~~ (1.17 cm^{-3}). These concentrations correspond to the presence of ~~regular strong winds and swell~~ strong regular winds and swells in the southern Indian Ocean that ~~generates significant primary emission. The average wind speeds calculated are 11.2, 8.8, and 4.3 m for the Southern Indian Ocean, Subtropical Indian Ocean, and continental group and 86 % of strong wind speed (> 20 m) events are found in the Southern Indian Ocean group. The differences in the sub-micron~~ generate significant primary emissions.

Significant differences are observed in the submicron modes between different ~~air mass types are visible both in the number concentration of aerosols, the mean diameters, and the standard deviation of the modes. Average number concentration of aerosols~~ types of air masses. The average aerosol number concentration is 830 cm^{-3} ~~in~~ for the Aitken mode and 240 cm^{-3} ~~in~~ for the accumulation mode. Continental air masses ~~exhibit the greatest number concentration of aerosols in the Aitken and accumulation modes with 1100 and~~ have concentrations of 1,100 cm^{-3} for the Aitken mode and 490 cm^{-3} ~~, respectively. Subtropical Indian Ocean air masses~~ for the accumulation mode. Similarly, the cleaner air masses from the subtropical Indian Ocean exhibit the lowest ~~number concentration of aerosols in the Aitken and accumulation modes~~ average concentrations, with 400 and 160 cm^{-3} ~~. Larger mean diameters are observed in the continental and Subtropical Indian Ocean groups with a similar value~~ for the Aitken ~~mode (45 and~~ and accumulation modes, respectively. Significant differences are also observed for the mean diameter. Air masses from the southern Indian Ocean, which are more influenced by primary emissions, have the smallest diameters: 37 ~~nm) and values of 120~~ nm for the Aitken mode and 97 nm for the accumulation mode. Larger mean diameters are observed in the continental and subtropical groups of the Indian Ocean. For the Aitken mode, the mean diameter is 45 and 37 nm, respectively. For the accumulation mode, the mean diameter is 120 and 143 ~~nm for the accumulation mode. Southern Indian Ocean air masses are characterized by lower mean diameters of 29~~ nm, respectively. The Aitken mode of the continental group has the largest average diameter, and there is no clear separation in terms of number concentration between this mode and ~~97 nm for the Aitken and accumulation modes. Considering that both Subtropical Indian Oceanand Southern Indian Ocean air masses are marine and minimally affected by terrestrial aerosols,~~ the ~~shift in the mean diametersof Subtropical Indian Ocean towards larger sizes may indicate that aerosols constituting this group have aged: the processes of coagulation and condensation had time to grow aerosols to larger sizes. Plus, the larger N in the Aitken mode of the continental air masses implies that there will be a more important coagulation process and therefore a less marked discontinuity between the Aitken and accumulation modes compared with cleaner air masses of the Subtropical Indian Oceangroup. On the opposite end, the position of the sub-micron modemean diameters of the Southern Indian Ocean group indicate newer primary marine aerosol emissions and less aging. The position of the sub-micron modes are in good agreement with the results obtained by Xu et al. (2021) and Kawana et al. (2022) who compared marine aerosol size distributions under continental influences and far from continental sources. In Kawana et al. (2022), the size distribution of terrestrial air masses exhibits a weak demarcation between the Aitken and the~~ accumulation mode~~making the size distribution more monomodal. For marine air masses, a clear bimodal size distribution is visible with a lower number concentration of aerosols in the Aitken and accumulation mode compared with terrestrial air masses . Xu et al. (2021) showed that clean air masses with high and low levels of biological activity exhibited a bimodal size distribution with an Aitken mode mean diameter ranging between 30-50 nm and an accumulation mode mean~~

~~diameter between 100-200 nm. In their study, polluted air masses with high and low levels of biological activity showed a more monomodal size distribution with a peak mean diameter between 50-60 nm~~This distinction is particularly noticeable when compared to air masses from the subtropical Indian Ocean group. This can be explained by the pollutant load (gases and aerosols) of the continental group, which favors growth through condensation and coagulation. In contrast, air masses from the subtropical Indian Ocean group are generally cleaner and therefore have less opportunity to grow.

7.2 Relationship between marine aerosol hygroscopicity, wind speed, and nanophytoplankton abundance

~~Sellegri et al. (2021) investigated the link between sea spray aerosol (SSA) fluxes and the abundance of phytoplankton cells of different nature (nanophytoplankton, picoplankton and coccolithophore-like cells) in surface seawater at different temperature. They found the strongest linear correlation between SSA and nanophytoplankton cells. In this section, the lowest and highest 5 % of κ values are not considered for the sake of statistical representativeness.~~

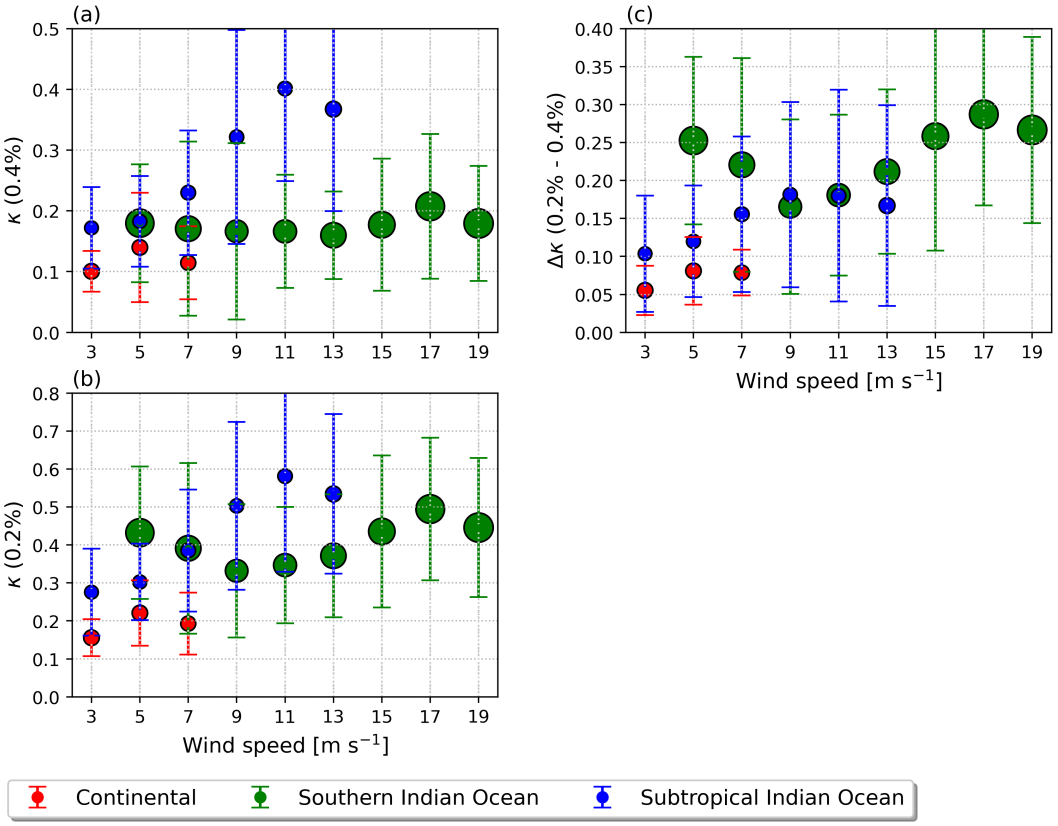

Figure 11. (~~left side~~a) κ at 0.4 % SS against wind speed. (~~right side~~b) κ at 0.2 % SS against wind speed. (c) Difference between κ at 0.2 % SS and 0.4 % SS against wind speed. Circles are the κ values averaged every 2 ~~m~~ m s^{-1}. Nanophytoplankton abundance is proportional to the size of the circles in ~~cells~~cells cm^{-3}.

~~Figure 8a shows~~ Figures 11a and 11b show the evolution of κ values at 0.2 and 0.4% SS and $\Delta\kappa$ as a function of local wind speed, local nanophytoplankton abundance, and the three types of air ~~mass. The average nanophytoplankton~~ masses. The difference in κ indicates the evolution of small particle hygroscopicity between the two activation diameters ($\sim$ 100 nm at 0.2% SS and $\sim$ 80 nm at 0.4% SS). Nanophytoplankton abundance values are ~~more elevated for the Southern~~ higher for the southern Indian Ocean group~~with an average value of 846.4~~ , with a mean value of 884.8 $\pm$ ~~518.9 cells , compared with average values of 282.3~~ 166.9 cells cm^{-3}, compared to a mean value of 267.4 $\pm$ ~~120.0 cells for the Subtropical~~ 29.6 cells cm^{-3} for the subtropical Indian Ocean group. ~~On the left panel, the~~ The separation between the three types of air masses is clearly visible~~, with the~~ . The highest average κ values ~~(0.24-0.4) for~~ are observed for air masses from the subtropical Indian Ocean, the ~~Subtropical Indian Oceanair masses, the smallest values for the Continental air masses(0.1-0.13)~~lowest for continental air masses, and intermediate values for ~~the Southern Indian Oceanair masses (0.17-0.22) .~~ air masses from the southern Indian Ocean. These results are consistent with previous observations of more polluted and hydrophobic air masses in the continental class, cleaner and more hydrophilic air masses in the subtropical Indian class, and intermediate air masses influenced by primary emissions (NaCl and organic) in the southern Indian Ocean class.

The effect of wind speed on hygroscopicity is clearly visible ~~for the Subtropical Indian Ocean, with~~ at both supersaturation for air masses from the subtropical Indian Ocean. κ values ~~increasing from 0.24 to 0.37~~ increase from 0.17 to 0.4 at 0.4% SS (from 0.28 to 0.58 at 0.2% SS) for wind speeds between 3 and ~~12 m .~~ 11 m s^{-1}. This result is consistent with the ~~low nanophytoplankton abundance~~ lower abundance of nanophytoplankton in this group, which makes the κ values ~~closer to NaCl κ. On the contrary, no trend between wind speed and~~ higher than those obtained for continental and southern Indian Ocean air masses, which brings the κ ~~is observed for air masses of~~ values closer to that of NaCl. $\Delta\kappa$ also increases from 0.1 to 0.18 between 3 and 9 m s^{-1}.

For air masses from the southern Indian Ocean~~group. Figure 8b shows the difference in~~ , at 0.2% SS, an increase in the average κ ~~between supersaturation at 0.2 and~~ values from 0.33 to 0.5 is observed between 9 and 17 m s^{-1}. At 0.4% ~~according to wind speed , phytoplankton abundance and air mass type. This difference in~~ SS, the κ ~~indicates the evolution of hygroscopicity for small particles between the two activation diameters. It is noteworthy that the Southern Indian Ocean group stands out from the two others. Hence,~~ value is stable with wind speed ($\sim$ 0.2). The effect of the ~~difference in κ between 0.2 % and~~ primary organic emissions in reducing the hygroscopicity, which counterbalances the increase in hygroscopicity caused by the NaCl emissions, is therefore clearly noticeable. This effect is particularly pronounced at 0.4% ~~SS according to the wind speed is the lowest (in average around 0) for the Continental and Subtropical Indian Ocean air masses, whereas it is between 0.1 and 0.3 for the Southern Indian Oceanair masses, with an increase in this difference when the wind speed increases from~~ supersaturation. $\Delta\kappa$ is higher for air masses from the southern Indian Ocean than for those from the subtropical Indian Ocean, and increases with increasing wind speed between 9 ~~to~~ and 17 ~~m . One difference between the three groups which could explain these features could be a significant amount of organic matter present in the aerosol of the Southern Indian Ocean group. Therefore the difference in κ for small particles of diameter between 76 nm and 104 nm is more pronounced in the regions of active biological production. The increase in the organic fraction towards smaller aerosol sizes has already been highlighted in O'Dowd et al. (2004), and is either possible due to~~ m s^{-1}. Thus, a more pronounced decrease in hygroscopicity is observed

for smaller aerosols with primary emissions in regions where phytoplankton is abundant. This observation suggests the presence of ~~primary marine organic aerosols (Schwier et al., 2015) or to the presence of volatile organic compounds which condenses in larger proportions on small sea salts. In the case of primary marine aerosols , O'Dowd et al. (2004) attribute the increasing organic enrichment of submicron aerosols with decreasing size to bubble-bursting processes when the ocean surface layer is more concentrated with surfactants which can be adsorbed at sea spray droplets surface~~a greater amount of organic matter on the surface of aerosol particles smaller than 100 nm compared to aerosols in the accumulation mode. This is ~~in agreement with previous studies (e.g. (Oppo et al., 1999)). In the case of secondary marine aerosols,~~ consistent with the ~~surface-to-volume ratioincreases when the size of aerosols decreases and provides the condensation of organic volatile compounds onto submicrometer particles (Mayer et al., 2020).~~ findings of Shulman et al. (1996); Oppo et al. (1999); Facchini et al. (2008) who observed that organic surfactants tend to accumulate on the surface of aerosols. Thus, for an identical NaCl/organic mass ratio, the proportion of organic matter on the surface will be greater for smaller aerosols.

~~8 Focus on particular events~~

~~Among the numerous situations observed during the 6 campaigns presented in this paper, several deserve to be detailed in order to analyze their origins or specific processes. Three types of situations have been selected (Fig. 9) which led to high aerosol observations with peaks above 3000 . The first corresponds to a polluted air mass observed during the SCRATCH campaign in northern Madagascar (Section 6.1). The second situation corresponds to a nucleation case of new particles in the marine atmospheric boundary layer observed during the OP3 campaign (Section 6.2). Finally, the last situation selected corresponds to a storm situation observed during SWINGS (Section 6.3),highlighting the primary production of aerosols and the evolution of their size distribution with air mass aging.~~

~~Position of the Marion Dufresne (thick lines) and 2-day back-trajectories (thin lines) from the FLEXPART model for the three selected situations, illustrating the origins of the air masses (1 dot per day).~~

8 Conclusions

~~8.1 Polluted case (SCRATCH)~~

~~Figure 10 shows the evolution of aerosol size distribution (e) and total aerosol and CO concentrations (f) between July 16~~ This paper presents and analyses aerosol measurements collected during six oceanographic campaigns conducted onboard the Marion Dufresne in the Indian and Southern Oceans in 2021 and ~~19, 2021. During this period, CO and aerosol concentration remains high (~~2023. The number of aerosols measured by the SMPS between 3 and 350 nm shows high variability, ranging from 50 to over 3,000 cm^{-3}. The highest concentrations (> ~~50 ppb and > 2000 ,respectively), showing that the area is generally affected by residual continental pollution. Several Na peaks exceeding 5000~~ 1,000 cm^{-3} ~~are also measured nighttime and are associated with a significant increase in CO concentrations by 10 to 15 ppb, indicating that the air mass is affected by additional pollution. Aerosol size distribution shows that the high average concentration observed during the period comes from the Aitken~~

mode (30 to 40 nm). It can also be seen that each peak is associated with the transport of a new nanoparticles mode (5 to 30 nm) and the growth of the Aitken mode to reach the accumulation mode (30 to 100 nm).) are observed in the Mozambique Channel. Back-trajectory analysis of Figure 9 (a,b,c,d) clearly indicates the passage of the air mass over the urbanized region of Majunga, located in north-western Madagascar. The altitude of the back-trajectory clearly indicates that the air mass sampled by the vessel is located above Madagascar between 800 m a.g.l. in the coastal zone and 1200 m a. g.l. in the center of the island, then subsides over the sea during transport. The time evolution of the mixed boundary layer (MBL) thickness over Madagascar, corrected for transport time, is shown in Figure 10g. There is an exceptional correlation of the MBL thickness with CO and Na peaks: each concentration peaks are associated with a MBL thickness greater than 800 m. This means that the pollution emitted over Madagascar has to be mixed in an atmospheric layer above 800 m to reach the ship. This can only happen in the afternoon when the MBL is sufficiently developed. Note that during this period, there is no rain at the Marion Dufresne location or along the back-trajectories to Madagascar (not shown here).

Temporal evolution of aerosol size distribution (e), aerosol number concentration (Na) and CO concentration (f) observed from July 16 to 19, 2021 (SCRATCH campaign, Fig. 1). Mixed boundary layer thickness evolution during 3 first hours over West of Madagascar along FLEXPART back-trajectories is presented in (g). Altitude of air masses along FLEXPART back-trajectories for the four CO peaks is visible in (a : 16-00 UTC, b : 16-18 UTC, c : 17-00 UTC, d : 18-01 UTC). The red squares correspond to the locations of the most urbanized areas in Majunga province (Madagascar).

8.1 Nucleation case (OP3)

Figure 11 shows the evolution of aerosol concentration (total number, size distribution and CCN) and ship track overlaid on cloud mask based on satellite brightness temperature (cloud areas correspond to brightness temperature lower than 282 K) (Janowiak et al., 2017b; Wang et al., 2017) on September 11th,2021.

Cloud cover and Marion Dufresne positions in (a, 02-06 UTC), (b, 06-10 UTC), (c, 10-14 UTC) and (d, 14-18 UTC). Temporal evolution of (e) aerosol size distribution and activation diameter at 0.2 and 0.4 % supersaturation and (f) aerosol concentration and cloud condensation nuclei at 0.2 and 0.4 % supersaturation observed during November 2, 2021 (OP3 campaign, Fig. 1).

Before 08:00 UTC (12 local time (LT)), SMPS measurements clearly showed two modes at 30 nm and 130 nm associated with a total concentration of 500 analysis showed that this region is strongly influenced by the advection of air masses from Africa or Madagascar. These high aerosol concentrations are therefore of the same order of magnitude as those reported by Flores et al. (2020) and Koponen et al. (2002) for polluted ocean air masses. Not surprisingly, the lowest aerosol concentrations are found in the regions furthest from the continents, generally between 100 and 1,000 cm^{-3}. The measured CCN number is low at 150 and 200 at 0.2 and

The number of CCN at 0.4% of SS, respectively. At 09:00 UTC, a strong increase of the total aerosols is observed reaching 4000 at 13:00 UTC. The SMPS showed a formation of new particles at 09:00 UTC (5 nm)associated with a classical banana-shaped growth (condensation-coagulation) typical to nucleation event ((Kulmala and Kerminen, 2008; Foucart et al., 2018; Määttänen et al., 2018) , and references therein). The activation diameters at 0.2 is much less variable, with concentrations between 60 and 0.4 % SS

are larger than the size of the nucleation mode. On the other hand, in parallel with the nucleation process, we observe a growth of the Aitken mode which goes from 30 nm to 80 nm and exceeds the activation diameter at 0.4 % SS. Thus the number of CCN at 0.4 % SS will go from 220 500 cm^{-3} (08:00 UTC) to 350 208 cm^{-3} (10:00 UTC) while on average), which is similar to the observations of Sanchez et al. (2021) or Humphries et al. (2021) in the same latitudinal ranges. The difference between the number of aerosols and the number of CCN at 0.2 % SS will remain globally stable during the day. Both processes of new particle formation and growth result from the formation of secondary oxidation products (like the oxidation of DMS and methanethiol (MeSH)in sulfuric acid) and are observed when UV is sufficient to form atmospheric oxidants (like hydroxyl radicals). From the satellite images in Figure 11 one can observe that the ship is located in a cloudy area until 07:00 UTC (11:00 LT) then passes into a clear sky area between 09:00 UTC and 15:00 UTC to pass again into a cloudy area. This passage corresponds exactly to the period of formation and growth of the particles. It is likely that the air mass was loaded with gaseous precursors before 07:00 UTC, which rapidly oxidized when the ship passed through clear skies, allowing the formation of low-volatile species. is particularly significant in the Mozambique Channel, with an N_{CCN}/N_{SMPS} ratio of about 0.17. This ratio can be explained by the presence of more hydrophobic aerosols associated with anthropogenic pollution advection ($\kappa < 0.1$). Conversely, in regions less influenced by continental air masses, this ratio can reach 0.65 with a fairly variable hygroscopicity parameter generally between 0.2 and 0.5, similar to the observations of Tatzelt et al. (2022).

8.1 Storm and aged case (SWINGS)

The last period highlighted corresponds to a case of primary emission of aerosols retained during the SWINGS campaign between March 2 at 00:00 UTC and 6 March at 00:00 UTC 2021. In Figure 12a,b,c,d are presented the back-trajectories of the air mass passing over the Marion Dufresne on 2 March at 06:00 UTC, 3 March at 00:00 UTC, and 3 March at 18:00 UTC projected onto a rain field (blue isolines) from the In order to explain the variability of marine aerosol concentrations, four situations have been analyzed using back-trajectories and ERA5 reanalyses. The color of the back trajectory analyses. The first situation corresponds to the 10 m wind speed of advection of a clean air mass located in the easternmost part of the measurement area. It has been observed that this type of air mass nearly evolves and that the Aiken and accumulation modes are not very pronounced. The activation diameter calculation is placed in a low concentration range close to the instrumental noise. The calculation of the hygroscopicity parameter is therefore particularly sensitive to the ERA5 fields along the trajectory. Figure 12d,e,f shows the temporal evolution of the size distribution, wave height, surface wind, total aerosol concentration, and hygroscopicity (κ).

10 m wind speed from ERA5 along 3 FLEXPART back-trajectories at three instant in (a), (b) and (c). Blues contours correspond to areas where rain rate is higher than 0.1 mm at that instant. Temporal evolution of (d) aerosol size distribution, (e) wind speed and wave height, (f) aerosol concentration and cloud condensation nuclei at 0.2 and 0.4 % supersaturation and (g) hygroscopicity parameters at 0.2 and 0.4 % supersaturation observed from March 2 to 5 2021 during SWINGS campaign (Fig. 1).

Three periods are identifiable. On March 2 before 06:00 UTC, the air mass came from the west in a windstorm zone with ERA5 wind speeds greater than 18 m over the previous 12 hours (Fig. 12a). The ship is affected by this storm since the measured

swell exceeds 14 m and the wind speed reaches 25 m . The air mass is however affected by rain which significantly limits aerosol concentrations particularly before 03:00 UTC (500 consistency between the CCN-100 and SMPS measurements. The second case illustrates the high N_{SMPS} values above 6,000 cm^{-3}). Hygroscopicity varies greatly with a measured κ fluctuating between 0.3 and 1. The second period from 2 March at 18:00 UTC and 3 March at 06:00 UTC corresponds to a phase of decreasing wind and swell conditions (Fig. 12b,d). On 2 March at 18:00 UTC, the Marion Dufresne moved approximately 300 km towards the northwest. The measured wind and swell conditions remain very high and the air mass has remained in heavy wind conditions greater than 20 m over the last 24 hours. However, according to ERA5 analyses, this air mass has not been affected by rain. Consequently, the aerosol concentrations measured on the Marion Dufresne exceed 3000 . Aerosol hygroscopicity has increased but remains quite fluctuating with a κ varying between 0.5 and 1 (Fig. 12g). The third period begins on 3 March at 06:00 UTC. SMPS data show the maintenance of a pronounced Aitken mode at around 30 nm and a concentration of around 2000 (Fig. 12d, f,g). There is also the formation of a second mode whose size increases over the period to reach a size characteristic of recorded in northern Madagascar. These concentration peaks have been shown to originate from layer 800 m above Madagascar, which then descends toward the Mozambique Channel. This variability has also been shown to be explained by the accumulation mode at around 100 nm. During the period, the Marion Dufresne continued its movement towards the northwest away from the storm area. On 3 March at 18:00 UTC, thickening of the mixing boundary layer in the urbanized coastal region of Madagascar, which allowed turbulent mixing of surface pollution in this upper layer. The third case corresponds to a period of storms between the Kerguelen and Reunion Islands. Paradoxically, the maximum aerosol concentration is offset from the maximum wind speed and wave height. Analysis of back-trajectories and precipitation fields from the ERA5 data show that the analyzes showed that during the storm passage the air mass was not affected by the rainand experienced moderate winds around 10 m during the previous day (Fig. 12e). Observations on board the Marion Dufresne show that sea conditions remained rough at least until 4 March at 06:00 UTC with swell fluctuating between 6 and 10 m (Fig. 12e). While the total aerosol concentration remained broadly stable over this period, it is notable that as the air mass aged, the hygroscopicity parameter gradually dropped from 0.7 on 3 March at 06:00 UTC to 0.2 on 5 March at 00:00 UTC (Fig. 12f,g). affected by rain, leading to a decrease of the aerosol concentration. As the ship approached Reunion Island and moved away from the storm, the aerosol concentrations increased to more than 3,000 cm^{-3}. These high concentrations were caused by the advection of an air mass that had not interacted with precipitation and had been under the influence of the storm 12 hours earlier, 100 km southwest of the ship. The fourth case corresponds to a sudden increase in aerosol concentration between Reunion Island and the Crozet Islands. Analysis of this period revealed a nucleation event followed by particle growth, which coincided with the moment when the Marion Dufresne passed from a cloudy area to a clear sky. Several studies have suggested that nucleation events are rare in the marine boundary layer and generally occur in the free troposphere (Covert et al., 1996; Bates et al., 1998; Humphries et al., 2016; Sanchez et al., 2021; Schmale et al., 2019; Williamson et al., 2019) . This case study is an example of a nucleation event observed in the open sea with an air mass that remained in the marine boundary layer.

Aerosol measurements collected during six oceanographic campaigns carried out in 2021 and 2023 within the Indian Ocean and the Southern Ocean on board the Marion Dufresne are presented and analyzed in this paper. SMPS data are used

~~to study the spatial distribution of Na over the sample area. Na shows a large variability with the highest concentrations observed either in tropical coastal regions or in the remote ocean and are attributable to large scale or local weather influences. CCN-100 measurements are used in collocation with SMPS measurements to study the activation ratio, activation diameter and hygroscopicity of aerosols at 0.2 and 0.4 % SS. The variability of the activation ratio allows to highlight differences in the chemical composition and size of the aerosols, which is confirmed by the spatial and temporal variability of the activation diameters and κ calculated according to Petters and Kreidenweis (2007). Globally the smaller aerosols activated between two activation diameters at 0.2 % and 0.4 % SS are more hydrophobic than those activated above the activation diameters at 0.2 % SS. κ values of organic species (0.22-0.24) are observed at 0.4 % SS during storm events occurring south of 35° S. In these areas, the nanophytoplankton cell abundance is more important than north of 35° S. As local weather conditions cannot fully explain the calculated κ, we performed 5-day back trajectories to access the air mass 's main~~

To generalize these results, a series of back-trajectory simulations were made for each hour of observation. Each air mass was then separated according to its origin: continental, ~~Subtropical Indian Ocean , or Southern~~ subtropical Indian Ocean or southern Indian Ocean. ~~The size distribution of aerosols according to the air masses origin shows significant differences that have already been highlighted in previous studies. We found that the aerosols transported by Subtropical Indian ocean air masses are more aged than that of Southern Indian Ocean~~ Similar to the case studies, we find that air masses ~~, which is traduced by larger Aitken and accumulation mode mean geometric diameters. The largest (lowest) number concentration of aerosols in the Aitken and accumulation modes is observed for continental (Subtropical Indian Ocean) size distribution . The highest numerical concentration of coarse mode aerosols is observed for the Southern Indian Ocean size distribution and is associated with rougher sea states and weather conditions (Tulet et al., 2024).~~ from the subtropical Indian Ocean are aged and less loaded with aerosols. This results in larger geometric diameters for the submicron modes. Conversely, air masses from the southern Indian Ocean have smaller geometric diameters, reflecting the effect of primary emissions of new particles due to stronger winds and higher wave heights. Note that the position of the submicron modes is in good agreement with the results obtained by Xu et al. (2021) and Kawana et al. (2022), who compared the size distributions of marine aerosols under polluted, clean, and marine biologically active conditions. The submicrometer aerosol size distribution of the continental group is characterized by the presence of an Aitken and an accumulation mode, in contrast to the monomodal size distribution observed by Flores et al. (2020). The number concentration of aerosols in the coarse mode is the highest for the southern Indian Ocean group, and is due to a more significant primary emission production in this region.

Additionally, from this classification, we investigated the possible relationship between the wind speed, the aerosol hygroscopicity (κ), and the nanophytoplankton abundance. Continental air masses are associated with more hydrophobic aerosols (κ from 0.1 to ~~0.13~~0.22), whereas ~~Subtropical~~ subtropical Indian Ocean air masses are associated with more hydrophilic aerosols (κ from ~~0.24 to 0.4~~0.17 to 0.6). Southern Indian Ocean air masses exhibit in-between values (κ from ~~0.17 to 0.22~~0.16 to 0.5). κ values of ~~Subtropical~~ subtropical Indian Ocean increase when the wind speed is getting stronger (from ~~5 to 12 m). A significant drop~~ 3 to 11 $\mathrm{m\,s^{-1}}$). These results show the effect of primary organic emissions on the decrease in κ in areas characterized by high phytoplankton concentrations, which counterbalances the increase in κ caused by NaCl emissions. This is consistent with previous studies highlighted by O'Dowd et al. (2004) or Schwier et al. (2015). A significant decrease in κ

(between 0.2 % and 0.4 % supersaturation) when the wind speed increases from 9 to 17 ~~m~~ $\mathrm{m\,s^{-1}}$ is observed for ~~Southern Indian Ocean air masses , and could be attributed~~ air masses originating the southern Indian Ocean. This phenomenon can be ascribed to the presence of a ~~more important~~ heightened concentration of organic species ~~at~~ on the surface of ~~the smaller aerosols. Finally, we focused on three situations. A polluted case during which high Na and CO concentrations are observed north of Madagascar during the night, and coincide with the passage of air masses into a well developed boundary layer over Madagascar before their subsidence towards the ship's location. A nucleation case followed by the growth of the particles which occurred north of Crozets islands, and coincides with the time when the Marion Dufresne passed from a cloudy to a clear sky area. A period between Kerguelen islands and Reunion island during which the ship encountered storm conditions, and was under the influence of air masses affected by rain, leading to a decrease in the aerosol number concentration. As the ship moved toward Reunion island, it went away from the strong wind and wave height conditions, and the air mass arriving at the ship's location were more aged, allowing the development of a stable Aitken mode, and an accumulation mode whose mean diameter moves towards larger diameters. These results give a view~~ smaller aerosols, which consequently leads to a reduction in the hygroscopic parameter.

This paper offers a large overview of the diversity of marine aerosols present in the ~~Indian and the Southern Oceanand highlight~~ subtropical and southern Indian Ocean, highlighting the variability of their hygroscopicity and CCN properties. This diversity ~~could be captured thanks to measurements realized over a long period of time and in~~ was revealed through measurements taken over an extended period and under various environmental conditions, ~~which supports the interest~~ thus confirming the value of the MAP-IO program. ~~The present work is based on 1.5 years of aerosol measurements and could further be developed in the future with a larger database~~These preliminary results can be further investigated over the course of several years as the program's database expands, enabling the characterization of the intraseasonal variability in marine aerosol properties.

These results also highlight the need to incorporate the variability of marine aerosol CCN properties into meteorological models, emphasizing the complexity of their characterization due to various coupled processes involving emissions, transport, aging, and chemical composition.

Appendix A: Air masses classification

A1

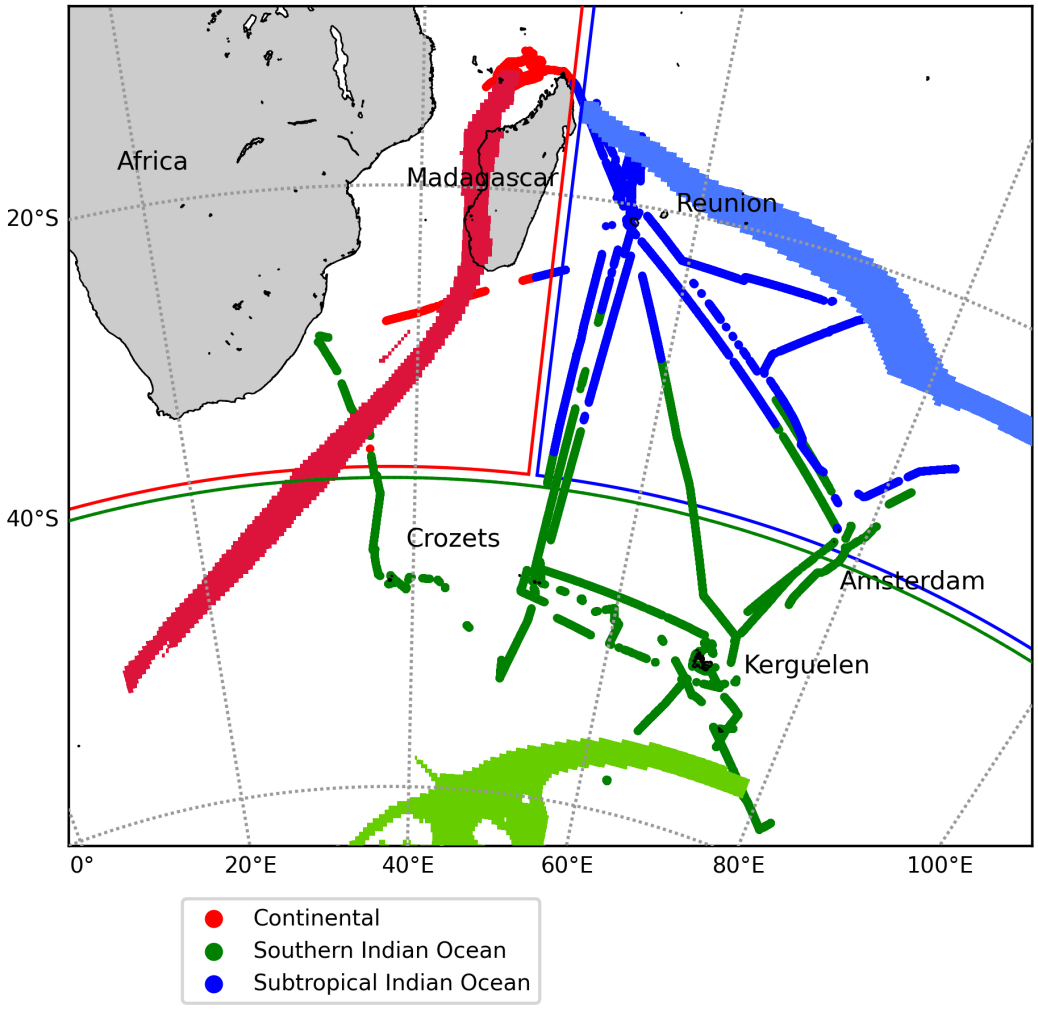

Figure A1. Classification of the aerosol data recorded in 2021 and 2023 according to the 5-days back-trajectories simulated by the FLEXPART model. Back-trajectories in red, blue and green are examples of continental, Subtropical Indian Ocean and Southern Indian Ocean air masses.

Data availability. Atmospheric data are available on the AERIS datacenter: https://www.aeris-data.fr/ (last access: 1 December 2024). Cytometry data are available on the SEANOE datacenter: https://www.seanoe.org/data/00783/89505/ (last access: 1 December 2024)

Author contributions. PT is the head of the MAP-IO program. JMM have been in charge of the installation and the maintenance of the instruments on-board. PT, JB are responsible for the aerosols in-situ data. MT supervised the installation of the Cytosense onboard the $MarionDufresne$. MT is responsible for the Cytosense scientific operations and instrument maintenance. MT analyzed and provided the phytoplankton data set. MD, PT are responsible for the aerosol data treatment. JP, JB set up the FLEXPART back-trajectories simulations. MD, PT, JP worked on the analysis of the aerosol, weather and phytoplankton in-situ data, and the FLEXPART outputs. MD, PT, JP worked on the paper's figures. GA verified the data treatment, filtering, and the calculation of the κ parameter

Competing interests. The contact author has declared that none of the authors has any competing interests.

Acknowledgements. The authors highly acknowledge the TAAF, IFREMER, LDAS, and GENAVIR for their help and constant support in the installation and the maintenance of all scientific instruments on board the Marion Dufresne. The authors also thank the technical teams of the LACy and OSU-R engaged in the data acquisition and the maintenance of the instruments of the MAP-IO program and the financial and human support of each laboratory partners such as OSU-R, LACy, LaMP, LAERO, LOA, LATMOS, LSCE, MIO, and ENTROPIE. MAP-IO is a scientific program led by the University of La Réunion and was funded by the European Union through the ERDF programme, the University of ~~La Réunion~~Reunion Island, the préfecture de ~~la Réunion~~Reunion Island, the Région Réunion, the CNRS, IFREMER, and the Flotte Océanographique Française. The authors also acknowledge Cyrielle Denjean and Sophia Brumer for the scientific discussions, and Vincent Noël for providing the satellite data.

References

Albrecht, B. A.: Aerosols, Cloud Microphysics, and Fractional Cloudiness, Science, 245, 1227–1230, https://doi.org/10.1126/science.245.4923.1227, 1989.

Andreae, M. O. and Rosenfeld, D.: Aerosol–cloud–precipitation interactions. Part 1. The nature and sources of cloud-active aerosols, Earth-Science Reviews, 89, 13–41, https://doi.org/10.1016/j.earscirev.2008.03.001, 2008.

Bae, S. Y., Park, R. J., Kim, Y. P., and Woo, J.-H.: Effects of below-cloud scavenging on the regional aerosol budget in East Asia, Atmospheric Environment, 58, 14–22, https://doi.org/10.1016/j.atmosenv.2011.08.065, 2012.

Bates, T. S., Kapustin, V. N., Quinn, P. K., Covert, D. S., Coffman, D. J., Mari, C., Durkee, P. A., De Bruyn, W. J., and Saltzman, E. S.: Processes controlling the distribution of aerosol particles in the lower marine boundary layer during the First Aerosol Characterization Experiment (ACE 1), Journal of Geophysical Research: Atmospheres, 103, 16 369–16 383, https://doi.org/10.1029/97JD03720, _eprint: https://onlinelibrary.wiley.com/doi/pdf/10.1029/97JD03720, 1998.

Bates, T. S., Quinn, P. K., Coffman, D. J., Johnson, J. E., and Middlebrook, A. M.: Dominance of organic aerosols in the marine boundary layer over the Gulf of Maine during NEAQS 2002 and their role in aerosol light scattering, Journal of Geophysical Research: Atmospheres, 110, https://doi.org/10.1029/2005JD005797, _eprint: https://onlinelibrary.wiley.com/doi/pdf/10.1029/2005JD005797, 2005.

Blain, S., Sarthou, G., and Laan, P.: Distribution of dissolved iron during the natural iron-fertilization experiment KEOPS (Kerguelen Plateau, Southern Ocean), Deep Sea Research Part II: Topical Studies in Oceanography, 55, 594–605, https://doi.org/10.1016/j.dsr2.2007.12.028, 2008.

Brioude, J., Cooper, O. R., Feingold, G., Trainer, M., Freitas, S. R., Kowal, D., Ayers, J. K., Prins, E., Minnis, P., McKeen, S. A., Frost, G. J., and Hsie, E.-Y.: Effect of biomass burning on marine stratocumulus clouds off the California coast, Atmospheric Chemistry and Physics, 9, 8841–8856, https://doi.org/10.5194/acp-9-8841-2009, publisher: Copernicus GmbH, 2009.

Carslaw, K. S., Lee, L. A., Reddington, C. L., Pringle, K. J., Rap, A., Forster, P. M., Mann, G. W., Spracklen, D. V., Woodhouse, M. T., Regayre, L. A., and Pierce, J. R.: Large contribution of natural aerosols to uncertainty in indirect forcing, Nature, 503, 67–71, https://doi.org/10.1038/nature12674, publisher: Nature Publishing Group, 2013.

Carslaw, K. S., Gordon, H., Hamilton, D. S., Johnson, J. S., Regayre, L. A., Yoshioka, M., and Pringle, K. J.: Aerosols in the Pre-industrial Atmosphere, Current Climate Change Reports, 3, 1–15, https://doi.org/10.1007/s40641-017-0061-2, 2017.

Cavalli, F., Facchini, M., Decesari, S., Mircea, M., Emblico, L., Fuzzi, S., Ceburnis, D., Yoon, Y., O'Dowd, C., Putaud, J.-P., et al.: Advances in characterization of size-resolved organic matter in marine aerosol over the North Atlantic, Journal of Geophysical Research: Atmospheres, 109, 2004.

Christiansen, S., Salter, M. E., Gorokhova, E., Nguyen, Q. T., and Bilde, M.: Sea Spray Aerosol Formation: Laboratory Results on the Role of Air Entrainment, Water Temperature, and Phytoplankton Biomass, Environmental Science & Technology, 53, 13 107–13 116, https://doi.org/10.1021/acs.est.9b04078, publisher: American Chemical Society, 2019.

Clarke, A., Kapustin, V., Howell, S., Moore, K., Lienert, B., Masonis, S., Anderson, T., and Covert, D.: Sea-Salt Size Distributions from Breaking Waves: Implications for Marine Aerosol Production and Optical Extinction Measurements during SEAS, Journal of Atmospheric and Oceanic Technology, 20, 1362–1374, https://doi.org/10.1175/1520-0426(2003)020<1362:SSDFBW>2.0.CO;2, publisher: American Meteorological Society Section: Journal of Atmospheric and Oceanic Technology, 2003.

Covert, D. S., Kapustin, V. N., Bates, T. S., and Quinn, P. K.: Physical properties of marine boundary layer aerosol particles of the mid-Pacific in relation to sources and meteorological transport, Journal of Geophysical Research: Atmospheres, 101, 6919–6930, https://doi.org/10.1029/95JD03068, 1996.

de Leeuw, G., Andreas, E. L., Anguelova, M. D., Fairall, C. W., Lewis, E. R., O'Dowd, C., Schulz, M., and Schwartz, S. E.: Production flux of sea spray aerosol, Reviews of Geophysics, 49, https://doi.org/10.1029/2010RG000349, _eprint: https://onlinelibrary.wiley.com/doi/pdf/10.1029/2010RG000349, 2011.

de Leeuw, G., Guieu, C., Arneth, A., Bellouin, N., Bopp, L., Boyd, P. W., van der Gon, H. A. C. D., Desboeufs, K. V., Dulac, F., Facchini, M. C., Gantt, B., Langmann, B., Mahowald, N. M., Marañón, E., O'Dowd, C., Olgun, N., Pulido-Villena, E., Rinaldi, M., Stephanou, E. G., and Wagener, T.: Ocean–Atmosphere Interactions of Particles, in: Ocean-Atmosphere Interactions of Gases and Particles, edited by Liss, P. S. and Johnson, M. T., pp. 171–246, Springer, Berlin, Heidelberg, ISBN 978-3-642-25643-1, https://doi.org/10.1007/978-3-642-25643-1_4, 2014.

Derkani, M. H., Alberello, A., Nelli, F., Bennetts, L. G., Hessner, K. G., MacHutchon, K., Reichert, K., Aouf, L., Khan, S., and Toffoli, A.: Wind, waves, and surface currents in the Southern Ocean: observations from the Antarctic Circumnavigation Expedition, Earth System Science Data, 13, 1189–1209, https://doi.org/10.5194/essd-13-1189-2021, 2021.

Dilmahamod, A. F., Penven, P., Aguiar-González, B., Reason, C. J. C., and Hermes, J. C.: A New Definition of the South-East Madagascar Bloom and Analysis of Its Variability, Journal of Geophysical Research: Oceans, 124, 1717–1735, https://doi.org/10.1029/2018JC014582, _eprint: https://onlinelibrary.wiley.com/doi/pdf/10.1029/2018JC014582, 2019.

El Yazidi, A., Ramonet, M., Ciais, P., Broquet, G., Pison, I., Abbaris, A., Brunner, D., Conil, S., Delmotte, M., Gheusi, F., Guerin, F., Hazan, L., Kachroudi, N., Kouvarakis, G., Mihalopoulos, N., Rivier, L., and Serça, D.: Identification of spikes associated with local sources in continuous time series of atmospheric CO, CO₂ and CH₄, Atmospheric Measurement Techniques, 11, 1599–1614, https://doi.org/10.5194/amt-11-1599-2018, 2018.

Facchini, M. C., Rinaldi, M., Decesari, S., Carbone, C., Finessi, E., Mircea, M., Fuzzi, S., Ceburnis, D., Flanagan, R., Nilsson, E. D., de Leeuw, G., Martino, M., Woeltjen, J., and O'Dowd, C. D.: Primary submicron marine aerosol dominated by insoluble organic colloids and aggregates, Geophysical Research Letters, 35, https://doi.org/10.1029/2008GL034210, _eprint: https://onlinelibrary.wiley.com/doi/pdf/10.1029/2008GL034210, 2008.

Flores, J. M., Bourdin, G., Altaratz, O., Trainic, M., Lang-Yona, N., Dzimban, E., Steinau, S., Tettich, F., Planes, S., Allemand, D., Agostini, S., Banaigs, B., Boissin, E., Boss, E., Douville, E., Forcioli, D., Furla, P., Galand, P. E., Sullivan, M. B., Gilson, , Lombard, F., Moulin, C., Pesant, S., Poulain, J., Reynaud, S., Romac, S., Sunagawa, S., Thomas, O. P., Troublé, R., Vargas, C. d., Thurber, R. V., Voolstra, C. R., Wincker, P., Zoccola, D., Bowler, C., Gorsky, G., Rudich, Y., Vardi, A., and Koren, I.: Tara Pacific Expedition's Atmospheric Measurements of Marine Aerosols across the Atlantic and Pacific Oceans: Overview and Preliminary Results, Bulletin of the American Meteorological Society, 101, E536–E554, https://doi.org/10.1175/BAMS-D-18-0224.1, publisher: American Meteorological Society Section: Bulletin of the American Meteorological Society, 2020.

Foucart, B., Sellegri, K., Tulet, P., Rose, C., Metzger, J.-M., and Picard, D.: High occurrence of new particle formation events at the Maïdo high-altitude observatory (2150 m), Réunion (Indian Ocean), Atmospheric Chemistry and Physics, 18, 9243–9261, https://doi.org/10.5194/acp-18-9243-2018, publisher: Copernicus GmbH, 2018.

Fragoso, G. M., Dallolio, A., Grant, S., Garrett, J. L., Ellingsen, I., Johnsen, G., and Johansen, T. A.: The Role of Rapid Changes in Weather on Phytoplankton Spring Bloom Dynamics From Mid-Norway Using Multiple Observational

Platforms, Journal of Geophysical Research: Oceans, 129, e2023JC020 415, https://doi.org/10.1029/2023JC020415, _eprint: https://onlinelibrary.wiley.com/doi/pdf/10.1029/2023JC020415, 2024.

Giglio, D. and Johnson, G. C.: Subantarctic and Polar Fronts of the Antarctic Circumpolar Current and Southern Ocean Heat and Freshwater Content Variability: A View from Argo, Journal of Physical Oceanography, 46, 749–768, https://doi.org/10.1175/JPO-D-15-0131.1, publisher: American Meteorological Society Section: Journal of Physical Oceanography, 2016.

Good, N., Topping, D. O., Allan, J. D., Flynn, M., Fuentes, E., Irwin, M., Williams, P. I., Coe, H., and McFiggans, G.: Consistency between parameterisations of aerosol hygroscopicity and CCN activity during the RHaMBLe discovery cruise, Atmos. Chem. Phys., 2010.

Heintzenberg, J., Covert, D. C., and Van Dingenen, R.: Size distribution and chemical composition of marine aerosols: a compilation and review, Tellus B, 52, 1104–1122, https://doi.org/10.1034/j.1600-0889.2000.00136.x, 2000.

Huang, S., Wu, Z., Wang, Y., Poulain, L., Höpner, F., Merkel, M., Herrmann, H., and Wiedensohler, A.: Aerosol Hygroscopicity and its Link to Chemical Composition in a Remote Marine Environment Based on Three Transatlantic Measurements, Environmental Science & Technology, 56, 9613–9622, https://doi.org/10.1021/acs.est.2c00785, publisher: American Chemical Society, 2022.

Humphries, R. S., Klekociuk, A. R., Schofield, R., Keywood, M., Ward, J., and Wilson, S. R.: Unexpectedly high ultrafine aerosol concentrations above East Antarctic sea ice, Atmospheric Chemistry and Physics, 16, 2185–2206, https://doi.org/10.5194/acp-16-2185-2016, 2016.

Humphries, R. S., Keywood, M. D., Gribben, S., McRobert, I. M., Ward, J. P., Selleck, P., Taylor, S., Harnwell, J., Flynn, C., Kulkarni, G. R., Mace, G. G., Protat, A., Alexander, S. P., and McFarquhar, G.: Southern Ocean latitudinal gradients of cloud condensation nuclei, Atmospheric Chemistry and Physics, 21, 12 757–12 782, https://doi.org/10.5194/acp-21-12757-2021, 2021.

IPCC: 2013 Clouds and Aerosols, in: Climate Change 2013 – The Physical Science Basis, edited by Intergovernmental Panel on Climate Change (IPCC), pp. 571–658, Cambridge University Press, 1 edn., ISBN 978-1-107-05799-9 978-1-107-66182-0 978-1-107-41532-4, https://doi.org/10.1017/CBO9781107415324.016, 2013.

IPCC: 2021 Short-lived Climate Forcers, in: Climate Change 2021 – The Physical Science Basis: Working Group I Contribution to the Sixth Assessment Report of the Intergovernmental Panel on Climate Change, edited by Intergovernmental Panel on Climate Change (IPCC), pp. 817–922, Cambridge University Press, Cambridge, ISBN 978-1-00-915788-9, https://doi.org/10.1017/9781009157896.008, 2021.

Janowiak, J., Joyce, B., and Xie, P.: NCEP/CPC L3 Half Hourly 4km Global (60S - 60N) Merged IR V1, https://doi.org/10.5067/P4HZB9N27EKU, edited by Andrey Savtchenko. Greenbelt, MD: Goddard Earth Sciences Data and Information Services Center (GES DISC). Accessed: [Data Access Date], 2017a.

Janowiak, J., Joyce, B., and Xie, P.: NCEP/CPC L3 Half Hourly 4km Global (60S - 60N) Merged IR V1, https://doi.org/10.5067/P4HZB9N27EKU, 2017b.

Jia, H., Ma, X., Yu, F., Liu, Y., and Yin, Y.: Distinct Impacts of Increased Aerosols on Cloud Droplet Number Concentration of Stratus/Stratocumulus and Cumulus, Geophysical Research Letters, 46, 13 517–13 525, https://doi.org/10.1029/2019GL085081, _eprint: https://onlinelibrary.wiley.com/doi/pdf/10.1029/2019GL085081, 2019.

Jung, E., Albrecht, B., Prospero, J. M., Jonsson, H. H., and Kreidenweis, S. M.: Vertical structure of aerosols, temperature, and moisture associated with an intense African dust event observed over the eastern Caribbean, Journal of Geophysical Research: Atmospheres, 118, 4623–4643, https://doi.org/10.1002/jgrd.50352, _eprint: https://onlinelibrary.wiley.com/doi/pdf/10.1002/jgrd.50352, 2013.

Kasparian, J., Hassler, C., Ibelings, B., Berti, N., Bigorre, S., Djambazova, V., Gascon-Diez, E., Giuliani, G., Houlmann, R., Kiselev, D., de Laborie, P., Le, A.-D., Magouroux, T., Neri, T., Palomino, D., Pfändler, S., Ray, N., Sousa, G., Staedler, D., Tettamanti, F., Wolf,

J.-P., and Beniston, M.: Assessing the Dynamics of Organic Aerosols over the North Atlantic Ocean, Scientific Reports, 7, 45 476, https://doi.org/10.1038/srep45476, publisher: Nature Publishing Group, 2017.

Kawana, K., Miyazaki, Y., Omori, Y., Tanimoto, H., Kagami, S., Suzuki, K., Yamashita, Y., Nishioka, J., Deng, Y., Yai, H., and Mochida, M.: Number-Size Distribution and CCN Activity of Atmospheric Aerosols in the Western North Pacific During Spring Pre-Bloom Period: Influences of Terrestrial and Marine Sources, Journal of Geophysical Research: Atmospheres, 127, e2022JD036 690, https://doi.org/10.1029/2022JD036690, _eprint: https://onlinelibrary.wiley.com/doi/pdf/10.1029/2022JD036690, 2022.

Koponen, I. K., Virkkula, A., Hillamo, R., Kerminen, V., and Kulmala, M.: Number size distributions and concentrations of marine aerosols: Observations during a cruise between the English Channel and the coast of Antarctica, Journal of Geophysical Research: Atmospheres, 107, https://doi.org/10.1029/2002JD002533, 2002.

Kristensen, T. B., Müller, T., Kandler, K., Benker, N., Hartmann, M., Prospero, J. M., Wiedensohler, A., and Stratmann, F.: Properties of cloud condensation nuclei (CCN) in the trade wind marine boundary layer of the western North Atlantic, Atmospheric Chemistry and Physics, 16, 2675–2688, https://doi.org/10.5194/acp-16-2675-2016, 2016.

Kulmala, M. and Kerminen, V.-M.: On the formation and growth of atmospheric nanoparticles, Atmospheric Research, 90, 132–150, https://doi.org/10.1016/j.atmosres.2008.01.005, 2008.

Kulmala, M., Laaksonen, A., and Pirjola, L.: Parameterizations for sulfuric acid/water nucleation rates, Journal of Geophysical Research: Atmospheres, 103, 8301–8307, https://doi.org/10.1029/97JD03718, _eprint: https://onlinelibrary.wiley.com/doi/pdf/10.1029/97JD03718, 1998.

Köhler, H.: The nucleus in and the growth of hygroscopic droplets, Trans. Faraday Soc., 32, 1152–1161, https://doi.org/10.1039/TF9363201152, 1936.

Lewis, E. R. and Schwartz, S. E.: Sea Salt Aerosol Production: Mechanisms, Methods, Measurements, and Models, American Geophysical Union, ISBN 978-0-87590-417-7, google-Books-ID: AEIo8ebgw00C, 2004.

Longhurst, A.: A major seasonal phytoplankton bloom in the Madagascar Basin, Deep Sea Research Part I: Oceanographic Research Papers, 48, 2413–2422, https://doi.org/10.1016/S0967-0637(01)00024-3, 2001.

Mallet, P.-, Pujol, O., Brioude, J., Evan, S., and Jensen, A.: Marine aerosol distribution and variability over the pristine Southern Indian Ocean, Atmospheric Environment, 182, 17–30, https://doi.org/10.1016/j.atmosenv.2018.03.016, 2018.

Mayer, K. J., Wang, X., Santander, M. V., Mitts, B. A., Sauer, J. S., Sultana, C. M., Cappa, C. D., and Prather, K. A.: Secondary Marine Aerosol Plays a Dominant Role over Primary Sea Spray Aerosol in Cloud Formation, ACS Central Science, 6, 2259–2266, https://doi.org/10.1021/acscentsci.0c00793, 2020.

McCoy, I. L., Bretherton, C. S., Wood, R., Twohy, C. H., Gettelman, A., Bardeen, C. G., and Toohey, D. W.: Influences of Recent Particle Formation on Southern Ocean Aerosol Variability and Low Cloud Properties, Journal of Geophysical Research: Atmospheres, 126, e2020JD033 529, https://doi.org/10.1029/2020JD033529, _eprint: https://onlinelibrary.wiley.com/doi/pdf/10.1029/2020JD033529, 2021.

Monahan, E. C., Spiel, D. E., and Davidson, K. L.: A Model of Marine Aerosol Generation Via Whitecaps and Wave Disruption, in: Oceanic Whitecaps: And Their Role in Air-Sea Exchange Processes, edited by Monahan, E. C. and Niocaill, G. M., pp. 167–174, Springer Netherlands, Dordrecht, ISBN 978-94-009-4668-2, https://doi.org/10.1007/978-94-009-4668-2_16, 1986.

Mondal, S., Lee, M.-A., Wang, Y.-C., and Semedi, B.: Long-term variation of sea surface temperature in relation to sea level pressure and surface wind speed in southern Indian Ocean, Journal of Marine Science and Technology, 29, 784–793, https://doi.org/10.51400/2709-6998.2558, 2022.

Moore, R. H., Karydis, V. A., Capps, S. L., Lathem, T. L., and Nenes, A.: Droplet number uncertainties associated with CCN: an assessment using observations and a global model adjoint, Atmospheric Chemistry and Physics, 13, 4235–4251, https://doi.org/10.5194/acp-13-4235-2013, 2013.

Määttänen, A., Merikanto, J., Henschel, H., Duplissy, J., Makkonen, R., Ortega, I. K., and Vehkamäki, H.: New Parameterizations for Neutral and Ion-Induced Sulfuric Acid-Water Particle Formation in Nucleation and Kinetic Regimes, Journal of Geophysical Research: Atmospheres, 123, 1269–1296, https://doi.org/10.1002/2017JD027429, _eprint: https://onlinelibrary.wiley.com/doi/pdf/10.1002/2017JD027429, 2018.

Novakov, T., Andreae, M. O., Gabriel, R., Kirchstetter, T. W., Mayol-Bracero, O. L., and Ramanathan, V.: Origin of carbonaceous aerosols over the tropical Indian Ocean: Biomass burning or fossil fuels?, Geophysical Research Letters, 27, 4061–4064, https://doi.org/10.1029/2000GL011759, _eprint: https://onlinelibrary.wiley.com/doi/pdf/10.1029/2000GL011759, 2000.

O'Dowd, C. D. and de Leeuw, G.: Marine aerosol production: a review of the current knowledge, Philosophical Transactions of the Royal Society A: Mathematical, Physical and Engineering Sciences, 365, 1753–1774, https://doi.org/10.1098/rsta.2007.2043, publisher: Royal Society, 2007.

O'Dowd, C. D., Smith, M. H., Consterdine, I. E., and Lowe, J. A.: Marine aerosol, sea-salt, and the marine sulphur cycle: a short review, Atmospheric Environment, 31, 73–80, https://doi.org/10.1016/S1352-2310(96)00106-9, 1997.

O'Dowd, C. D., Facchini, M. C., Cavalli, F., Ceburnis, D., Mircea, M., Decesari, S., Fuzzi, S., Yoon, Y. J., and Putaud, J.-P.: Biogenically driven organic contribution to marine aerosol, Nature, 431, 676–680, https://doi.org/10.1038/nature02959, 2004.

Oppo, C., Bellandi, S., Degli Innocenti, N., Stortini, A. M., Loglio, G., Schiavuta, E., and Cini, R.: Surfactant components of marine organic matter as agents for biogeochemical fractionation and pollutant transport via marine aerosols, Marine Chemistry, 63, 235–253, https://doi.org/10.1016/S0304-4203(98)00065-6, 1999.

Ovadnevaite, J., Manders, A., De Leeuw, G., Ceburnis, D., Monahan, C., Partanen, A.-I., Korhonen, H., and O'Dowd, C. D.: A sea spray aerosol flux parameterization encapsulating wave state, Atmospheric Chemistry and Physics, 14, 1837–1852, https://doi.org/10.5194/acp-14-1837-2014, 2014.

Pant, V., Deshpande, C. G., and Kamra, A. K.: The concentration and number size distribution measurements of the Marine Boundary Layer aerosols over the Indian Ocean, Atmospheric Research, 92, 381–393, https://doi.org/10.1016/j.atmosres.2008.12.004, 2009.

Petters, M. D. and Kreidenweis, S. M.: A single parameter representation of hygroscopic growth and cloud condensation nucleus activity, Atmospheric Chemistry and Physics, 7, 1961–1971, https://doi.org/10.5194/acp-7-1961-2007, publisher: Copernicus GmbH, 2007.

Pisso, I., Sollum, E., Grythe, H., Kristiansen, N. I., Cassiani, M., Eckhardt, S., Arnold, D., Morton, D., Thompson, R. L., Groot Zwaaftink, C. D., Evangeliou, N., Sodemann, H., Haimberger, L., Henne, S., Brunner, D., Burkhart, J. F., Fouilloux, A., Brioude, J., Philipp, A., Seibert, P., and Stohl, A.: The Lagrangian particle dispersion model FLEXPART version 10.4, Geoscientific Model Development, 12, 4955–4997, https://doi.org/10.5194/gmd-12-4955-2019, publisher: Copernicus GmbH, 2019.

Pringle, K. J., Tost, H., Pozzer, A., Pöschl, U., and Lelieveld, J.: Global distribution of the effective aerosol hygroscopicity parameter for CCN activation, Atmospheric Chemistry and Physics, 10, 5241–5255, https://doi.org/10.5194/acp-10-5241-2010, 2010.

Quinn, P. K., Coffman, D. J., Johnson, J. E., Upchurch, L. M., and Bates, T. S.: Small fraction of marine cloud condensation nuclei made up of sea spray aerosol, Nature Geoscience, 10, 674–679, https://doi.org/10.1038/ngeo3003, publisher: Nature Publishing Group, 2017.

Ramanathan, V., Crutzen, P. J., Lelieveld, J., Mitra, A. P., Althausen, D., Anderson, J., Andreae, M. O., Cantrell, W., Cass, G. R., Chung, C. E., Clarke, A. D., Coakley, J. A., Collins, W. D., Conant, W. C., Dulac, F., Heintzenberg, J., Heymsfield, A. J., Holben, B., Howell, S., Hudson, J., Jayaraman, A., Kiehl, J. T., Krishnamurti, T. N., Lubin, D., McFarquhar, G., Novakov, T., Ogren, J. A., Podgorny,

I. A., Prather, K., Priestley, K., Prospero, J. M., Quinn, P. K., Rajeev, K., Rasch, P., Rupert, S., Sadourny, R., Satheesh, S. K., Shaw, G. E., Sheridan, P., and Valero, F. P. J.: Indian Ocean Experiment: An integrated analysis of the climate forcing and effects of the great Indo-Asian haze, Journal of Geophysical Research: Atmospheres, 106, 28 371–28 398, https://doi.org/10.1029/2001JD900133, _eprint: https://onlinelibrary.wiley.com/doi/pdf/10.1029/2001JD900133, 2001.

Roberts, G. C., Day, D. A., Russell, L. M., Dunlea, E. J., Jimenez, J. L., Tomlinson, J. M., Collins, D. R., Shinozuka, Y., and Clarke, A. D.: Characterization of particle cloud droplet activity and composition in the free troposphere and the boundary layer during INTEX-B, Atmospheric Chemistry and Physics, 10, 6627–6644, https://doi.org/10.5194/acp-10-6627-2010, 2010.

Saltzman, E. S.: Marine Aerosols, https://doi.org/10.1029/2008GM000769, 2009.

Sanchez, K. J., Roberts, G. C., Saliba, G., Russell, L. M., Twohy, C., Reeves, J. M., Humphries, R. S., Keywood, M. D., Ward, J. P., and McRobert, I. M.: Measurement report: Cloud processes and the transport of biological emissions affect southern ocean particle and cloud condensation nuclei concentrations, Atmospheric Chemistry and Physics, 21, 3427–3446, https://doi.org/10.5194/acp-21-3427-2021, publisher: Copernicus GmbH, 2021.

Sandu, I., Brenguier, J.-L., Geoffroy, O., Thouron, O., and Masson, V.: Aerosol Impacts on the Diurnal Cycle of Marine Stratocumulus, Journal of the Atmospheric Sciences, 65, 2705–2718, https://doi.org/10.1175/2008JAS2451.1, 2008.

Schmale, J., Baccarini, A., Thurnherr, I., Henning, S., Efraim, A., Regayre, L., Bolas, C., Hartmann, M., Welti, A., Lehtipalo, K., Aemisegger, F., Tatzelt, C., Landwehr, S., Modini, R. L., Tummon, F., Johnson, J. S., Harris, N., Schnaiter, M., Toffoli, A., Derkani, M., Bukowiecki, N., Stratmann, F., Dommen, J., Baltensperger, U., Wernli, H., Rosenfeld, D., Gysel-Beer, M., and Carslaw, K. S.: Overview of the Antarctic Circumnavigation Expedition: Study of Preindustrial-like Aerosols and Their Climate Effects (ACE-SPACE), Bulletin of the American Meteorological Society, 100, 2260–2283, https://doi.org/10.1175/BAMS-D-18-0187.1, publisher: American Meteorological Society Section: Bulletin of the American Meteorological Society, 2019.

Schott, F. A., Xie, S., and McCreary, J. P.: Indian Ocean circulation and climate variability, Reviews of Geophysics, 47, 2007RG000 245, https://doi.org/10.1029/2007RG000245, 2009.

Schulz, M., Prospero, J. M., Baker, A. R., Dentener, F., Ickes, L., Liss, P. S., Mahowald, N. M., Nickovic, S., García-Pando, C. P., Rodríguez, S., Sarin, M., Tegen, I., and Duce, R. A.: Atmospheric Transport and Deposition of Mineral Dust to the Ocean: Implications for Research Needs, Environmental Science & Technology, 46, 10 390–10 404, https://doi.org/10.1021/es300073u, 2012.

Schwier, A. N., Rose, C., Asmi, E., Ebling, A. M., Landing, W. M., Marro, S., Pedrotti, M.-L., Sallon, A., Iuculano, F., Agusti, S., Tsiola, A., Pitta, P., Louis, J., Guieu, C., Gazeau, F., and Sellegri, K.: Primary marine aerosol emissions from the Mediterranean Sea during pre-bloom and oligotrophic conditions: correlations to seawater chlorophyll <i>a</i> from a mesocosm study, Atmospheric Chemistry and Physics, 15, 7961–7976, https://doi.org/10.5194/acp-15-7961-2015, 2015.

Sciare, J., Favez, O., Sarda-Estève, R., Oikonomou, K., Cachier, H., and Kazan, V.: Long-term observations of carbonaceous aerosols in the Austral Ocean atmosphere: Evidence of a biogenic marine organic source, Journal of Geophysical Research: Atmospheres, 114, 2009.

Sedwick, P. N., Blain, S., Quéguiner, B., Griffiths, F. B., Fiala, M., Bucciarelli, E., and Denis, M.: Resource limitation of phytoplankton growth in the Crozet Basin, Subantarctic Southern Ocean, Deep Sea Research Part II: Topical Studies in Oceanography, 49, 3327–3349, https://doi.org/10.1016/S0967-0645(02)00086-3, 2002.

Sellegri, K., Nicosia, A., Freney, E., Uitz, J., Thyssen, M., Grégori, G., Engel, A., Zäncker, B., Haëntjens, N., Mas, S., Picard, D., Saint-Macary, A., Peltola, M., Rose, C., Trueblood, J., Lefevre, D., D'Anna, B., Desboeufs, K., Meskhidze, N., Guieu, C., and Law, C. S.: Surface ocean microbiota determine cloud precursors, Scientific Reports, 11, 281, https://doi.org/10.1038/s41598-020-78097-5, publisher: Nature Publishing Group, 2021.

Sellegri, K., Harvey, M., Peltola, M., Saint-Macary, A., Barthelmeß, T., Rocco, M., Moore, K. A., Cristi, A., Peyrin, F., Barr, N., Labonnote, L., Marriner, A., McGregor, J., Safi, K., Deppeler, S., Archer, S., Dunne, E., Harnwell, J., Delanoe, J., Freney, E., Rose, C., Bazantay, C., Planche, C., Saiz-Lopez, A., Quintanilla-López, J. E., Lebrón-Aguilar, R., Rinaldi, M., Banson, S., Joseph, R., Lupascu, A., Jourdan, O., Mioche, G., Colomb, A., Olivares, G., Querel, R., McDonald, A., Plank, G., Bukosa, B., Dillon, W., Pelon, J., Baray, J.-L., Tridon, F., Donnadieu, F., Szczap, F., Engel, A., DeMott, P. J., and Law, C. S.: Sea2Cloud: From Biogenic Emission Fluxes to Cloud Properties in the Southwest Pacific, Bulletin of the American Meteorological Society, 104, E1017–E1043, https://doi.org/10.1175/BAMS-D-21-0063.1, publisher: American Meteorological Society Section: Bulletin of the American Meteorological Society, 2023.

Shulman, M. L., Jacobson, M. C., Carlson, R. J., Synovec, R. E., and Young, T. E.: Dissolution behavior and surface tension effects of organic compounds in nucleating cloud droplets, Geophysical Research Letters, 23, 277–280, 1996.

Simpkins, G.: Aerosol–cloud interactions, Nature Climate Change, 8, 457–457, https://doi.org/10.1038/s41558-018-0195-9, publisher: Nature Publishing Group, 2018.

Stevens, B., Cotton, W. R., and Feingold, G.: A critique of one- and two-dimensional models of boundary layer clouds with a binned representations of drop microphysics, Atmospheric Research, 47-48, 529–553, https://doi.org/10.1016/S0169-8095(98)00059-3, 1998.

Su, B., Wang, T., Zhang, G., Liang, Y., Lv, C., Hu, Y., Li, L., Zhou, Z., Wang, X., and Bi, X.: A review of atmospheric aging of sea spray aerosols: Potential factors affecting chloride depletion, Atmospheric Environment, 290, 119 365, https://doi.org/10.1016/j.atmosenv.2022.119365, 2022.

Tatzelt, C., Henning, S., Welti, A., Baccarini, A., Hartmann, M., Gysel-Beer, M., van Pinxteren, M., Modini, R. L., Schmale, J., and Stratmann, F.: Circum-Antarctic abundance and properties of CCN and INPs, Atmospheric Chemistry and Physics, 22, 9721–9745, https://doi.org/10.5194/acp-22-9721-2022, publisher: Copernicus GmbH, 2022.

Textor, C., Schulz, M., Guibert, S., Kinne, S., Balkanski, Y., Bauer, S., Berntsen, T., Berglen, T., Boucher, O., Chin, M., Dentener, F., Diehl, T., Easter, R., Feichter, H., Fillmore, D., Ghan, S., Ginoux, P., Gong, S., Grini, A., Hendricks, J., Horowitz, L., Huang, P., Isaksen, I., Iversen, T., Kloster, S., Koch, D., Kirkeva, A., Kristjansson, J. E., Krol, M., Lauer, A., Lamarque, J. F., Liu, X., Montanaro, V., Myhre, G., Penner, J., Pitari, G., Reddy, S., Seland, , Stier, P., Takemura, T., and Tie, X.: Analysis and quantification of the diversities of aerosol life cycles within AeroCom, Atmos. Chem. Phys., 2006.

Tulet, P., Van Baelen, J., Bosser, P., Brioude, J., Colomb, A., Goloub, P., Pazmino, A., Portafaix, T., Ramonet, M., Sellegri, K., Thyssen, M., Gest, L., Marquestaut, N., Mékiès, D., Metzger, J.-M., Athier, G., Blarel, L., Delmotte, M., Desprairies, G., Dournaux, M., Dubois, G., Duflot, V., Lamy, K., Gardes, L., Guillemot, J.-F., Gros, V., Kolasinski, J., Lopez, M., Magand, O., Noury, E., Nunes-Pinharanda, M., Payen, G., Pianezze, J., Picard, D., Picard, O., Prunier, S., Rigaud-Louise, F., Sicard, M., and Torres, B.: MAP-IO, an atmospheric and marine observatory program onboard Marion Dufresne over the Southern Ocean, https://doi.org/10.5194/essd-2023-531, 2024.

Twomey, S.: Pollution and the planetary albedo, Atmospheric Environment (1967), 8, 1251–1256, https://doi.org/10.1016/0004-6981(74)90004-3, 1974.

Twomey, S.: The Influence of Pollution on the Shortwave Albedo of Clouds, Journal of the Atmospheric Sciences, 34, 1149–1152, https://doi.org/10.1175/1520-0469(1977)034<1149:TIOPOT>2.0.CO;2, publisher: American Meteorological Society Section: Journal of the Atmospheric Sciences, 1977.

Wall, C. J., Storelvmo, T., and Possner, A.: Global observations of aerosol indirect effects from marine liquid clouds, Atmospheric Chemistry and Physics, 23, 13 125–13 141, https://doi.org/10.5194/acp-23-13125-2023, 2023.

Wang, Y., Zheng, X., Dong, X., Xi, B., Wu, P., Logan, T., and Yung, Y. L.: Impacts of long-range transport of aerosols on marine-boundary-layer clouds in the eastern North Atlantic, Atmospheric Chemistry and Physics, 20, 14 741–14 755, https://doi.org/10.5194/acp-20-14741-2020, 2020.

Wang, Z., Zhong, R., Lai, C., and Chen, J.: Evaluation of the GPM IMERG satellite-based precipitation products and the hydrological utility, Atmospheric Research, 196, 151–163, https://doi.org/10.1016/j.atmosres.2017.06.020, 2017.

Warren, S. G., Hahn, C. J., London, J., Chervin, R. M., and Jenne, R. L.: Global distribution of total cloud cover and cloud type amounts over the ocean, Tech. Rep. DOE/ER-0406; NCAR/TN-317-STR, USDOE Office of Energy Research, Washington, DC (USA). Carbon Dioxide Research Div.; National Center for Atmospheric Research, Boulder, CO (USA), https://doi.org/10.2172/5415329, 1988.

Warren, S. G., Eastman, R. M., and Hahn, C. J.: A Survey of Changes in Cloud Cover and Cloud Types over Land from Surface Observations, 1971–96, Journal of Climate, 20, 717–738, https://doi.org/10.1175/JCLI4031.1, publisher: American Meteorological Society Section: Journal of Climate, 2007.

Wex, H., Dieckmann, K., Roberts, G. C., Conrath, T., Izaguirre, M. A., Hartmann, S., Herenz, P., Schäfer, M., Ditas, F., Schmeissner, T., Henning, S., Wehner, B., Siebert, H., and Stratmann, F.: Aerosol arriving on the Caribbean island of Barbados: physical properties and origin, Atmospheric Chemistry and Physics, 16, 14 107–14 130, https://doi.org/10.5194/acp-16-14107-2016, 2016.

Williamson, C. J., Kupc, A., Axisa, D., Bilsback, K. R., Bui, T., Campuzano-Jost, P., Dollner, M., Froyd, K. D., Hodshire, A. L., Jimenez, J. L., Kodros, J. K., Luo, G., Murphy, D. M., Nault, B. A., Ray, E. A., Weinzierl, B., Wilson, J. C., Yu, F., Yu, P., Pierce, J. R., and Brock, C. A.: A large source of cloud condensation nuclei from new particle formation in the tropics, Nature, 574, 399–403, https://doi.org/10.1038/s41586-019-1638-9, publisher: Nature Publishing Group, 2019.

Xu, W., Fossum, K. N., Ovadnevaite, J., Lin, C., Huang, R.-J., O'Dowd, C., and Ceburnis, D.: The impact of aerosol size-dependent hygroscopicity and mixing state on the cloud condensation nuclei potential over the north-east Atlantic, Atmospheric Chemistry and Physics, 21, 8655–8675, https://doi.org/10.5194/acp-21-8655-2021, publisher: Copernicus GmbH, 2021.

Yoon, Y. J., Ceburnis, D., Cavalli, F., Jourdan, O., Putaud, J. P., Facchini, M. C., Decesari, S., Fuzzi, S., Sellegri, K., Jennings, S. G., and O'Dowd, C. D.: Seasonal characteristics of the physicochemical properties of North Atlantic marine atmospheric aerosols, Journal of Geophysical Research: Atmospheres, 112, https://doi.org/10.1029/2005JD007044, _eprint: https://onlinelibrary.wiley.com/doi/pdf/10.1029/2005JD007044, 2007.

Young, I.: Seasonal variability of the global ocean wind and wave climate, International Journal of Climatology, 19, 931–950, https://doi.org/10.1002/(SICI)1097-0088(199907)19:9<931::AID-JOC412>3.0.CO;2-O, 1999.

Zheng, G., Wang, Y., Wood, R., Jensen, M. P., Kuang, C., McCoy, I. L., Matthews, A., Mei, F., Tomlinson, J. M., Shilling, J. E., Zawadowicz, M. A., Crosbie, E., Moore, R., Ziemba, L., Andreae, M. O., and Wang, J.: New particle formation in the remote marine boundary layer, Nature Communications, 12, 527, https://doi.org/10.1038/s41467-020-20773-1, publisher: Nature Publishing Group, 2021.